

Numerical Modelling and Parametric Assessment of Hybrid Flat Slabs with Steel Shear Heads

D.V. Bompa, A. Y. Elghazouli

Department of Civil and Environmental Engineering, Imperial College London, UK

Abstract

This investigation examines the performance of hybrid reinforced concrete flat slabs, incorporating fully-integrated shear-heads at connections to steel columns, through a series of numerical evaluations and parametric studies. Validations of the adopted nonlinear finite element procedures, which employ concrete damage plasticity constitutive models, are carried out against experimental results on hybrid members. Complementary verifications on conventional reinforced concrete flat slabs are also undertaken to ensure the reliability of the selected ranges for key modelling parameters. Comparison of the numerical simulations against the test results shows close correlations in terms of ultimate strength, deformations and stress levels in the constituent elements of hybrid members. This is followed by a series of parametric assessments on key structural parameters for hybrid flat slabs with steel shear heads. The results of these investigations enable the identification of three modes of failure as a function of the interaction between the shear-head and surrounding concrete. The findings permit the development of improved analytical models for predicting the response as well as ultimate strength of such members. In addition, recommendations are given for the determination of shear-head dependent parameters, which are required for practical design purposes, with particular focus on the embedment length and section size of the shear-head elements. The suggested expressions for assessing the shear-head characteristics offer a more reliable design approach in comparison with existing methods and are suitable for effective practical application and implementation in codified procedures.

Keywords: RC flat slabs; hybrid steel/concrete; fully-integrated shear-heads; numerical modelling; rotational response; ultimate behaviour

**Corresponding Author:*

Prof. A. Y. Elghazouli, Dept. of Civil & Environmental Engineering, Imperial College London, UK.
Email: a.elghazouli@imperial.ac.uk

1. Introduction

Shear-head systems are often used in reinforced concrete (RC) floors either for strength enhancement or to enable connection to steel columns. A number of previous studies have examined the effectiveness of shear-heads in various configurations against punching shear in RC flat slabs [e.g. 1-5]. Several recent investigations on such hybrid systems have employed fully integrated cruciform shear-heads connected to tubular columns [6-8]. The assemblages typically consisted of four I-shaped steel profiles with various lengths welded to the four faces of the rectangular columns. It was shown [8] that the punching shear strength can be significantly enhanced in comparison with conventional RC flat slabs. Hybrid steel/column assemblages employing partially-embedded steel inserts, in which a gap is introduced around the column to ensure ductile bare-steel shear-head behaviour, was also examined [8].

A recent study by the authors examined experimentally the effectiveness of headed stud reinforcement in hybrid slabs with fully integrated shear-heads [9]. The test results enabled the development of analytical models that depict the rotational response, flexural strength and punching shear strength as a function of the shear-head embedment length, layout and section size, yet only general suggestions for the design of the steel insert were given. Related studies were also carried on the shear transfer mechanisms and failure criteria in one-way hybrid members (i.e. RC beams with fully-embedded shear-heads connected to steel columns), including numerical and experimental assessments [10-12]. These studies focused primarily on the ultimate behaviour of the RC-to-steel interface region, rather than on developing detailed expressions for the design of the shear-heads.

Although various numerical investigations on RC flat slabs exist [13-16], very few report the use of concrete damage plasticity (CDP) models in simulations [17-19] and they are generally validated against a limited number of tests with identical or similar geometries. For example, nonlinear finite element (FE) analysis of relatively thin RC flat slabs subjected to static and pseudo-dynamic loading was undertaken in order to investigate failure modes and cracking patterns [17]; the material parameters in CDP were in this case calibrated based on test results of an interior slab-column connection. Another FE modelling study [18] investigating the punching shear capacity of flat slabs strengthened with concrete screws showed poor prediction of the structural stiffness, primarily due to the inadequacy of the crack model employed in the simulations. A parametric study was also carried out [19] in which

assessments of the elastic stress fields that develop within interior slab-to-column connections were carried out, with validation against a specimen which failed in flexural punching.

Detailed numerical studies on hybrid steel-concrete flat slabs are relatively limited [20, 21]. Analysis and parametric assessments on hybrid and RC slab tests [1, 8] were carried out to highlight the influence of key parameters which govern the performance of steel shear-heads in flat slabs [20]. Numerical simulations on hybrid steel tubular column/flat slab configurations with very short shear-heads [21] also indicated that, for assessments of punching shear strength, the shear-head system can be treated as an enlarged column. However, previous studies were limited to specific ranges and their scope was not adequate to enable the development of guidance and procedures which are suitable for practical application. They either assess the efficiency of existing models for RC members [1, 20], or propose equations that are developed from rigid shear-head behaviour characteristic for very short embedment lengths [21].

A model, modified for connections between RC flat slabs to CFT columns by means of shear-heads, exists [7]. It considers the same force distribution obtained from RC flat-slab column behaviour [1] and an empirically determined factor to assess the contribution of the shear-head to the punching shear strength of the member. All existing methods [7, 20] are however validated on a limited range of tests with similar structural parameters that cover specific ultimate behaviour characteristics. These methods become unreliable for design situations outside the validated ranges.

This paper investigates the performance of shear-head systems in hybrid RC flat slab-to-steel column systems through a series of numerical parametric assessments in which key geometric and material parameters are varied. Numerical simulations are carried out using nonlinear finite element procedures which are validated against tests on conventional RC flat slabs [22] as well as hybrid configurations tested by the authors [9]. The tests considered showed failure modes ranging from flexure to punching shear, and included a wide range of structural parameters and geometries. Detailed sensitivity and parametric investigations are undertaken to provide detailed insights into the physical behaviour for a wide range of hybrid configurations outside of the existing test database [6-9]. Within the parametric investigations, parametric assessments were carried out to assess the influence of the shear-head embedment length, section size, slab flexibility, slab bending effective depth, as well as

the concrete strength on the behaviour of hybrid slabs. The numerical results obtained enable a direct assessment of the ultimate behaviour in terms of both strength and deformation characteristics.

The findings from the numerical investigations undertaken in this study, in conjunction with the experimental results, provide reliable validation and further refinement for recent analytical models applicable to a wide range of hybrid slabs proposed by the authors [9]. The rotational response and ultimate strength assessments obtained from the simulations are used for the calibration and improvement of a bi-linear rotational model which was initially validated based on a limited number of available tests [6-9]. Key observations from the numerical simulations also enable the definition of shear-head dependent parameters required for the design of hybrid assemblages incorporating shear-heads, with focus on the design of shear-head embedment length l_v and section size. In conjunction with punching shear design and assessment methods for hybrid flat slabs, which are developed from established RC approaches [23, 24], new expressions for the design of the embedment length and section size of the shear-head in terms of section moment of inertia, shear active area, as well as shear-head width and depth, are proposed. Additionally, relationships to assess the bending moment at which yielding occurs in the shear-head flange, as a fraction of its plastic capacity, are also proposed. Finally, practical considerations regarding the design of the shear-head are highlighted. Considering the wide range of salient parameters accounted for within the parametric investigations, and which are also used for analytical validation, these relationships offer a more reliable design approach in comparison with existing methods. The proposed expressions for assessing the shear-head characteristics, as well as the ultimate strength of the hybrid members, are suitable for practical application and implementation in codified procedures.

2. Numerical Simulations

This section describes numerical simulations and validations carried out using the finite element program ABAQUS [25] in order to obtain detailed insights into the structural behaviour of RC flat slabs provided with shear heads which are welded directly to steel columns. The section first discusses the constitutive models adopted for concrete, reinforcement and structural steel. It then describes the validations carried out against the

experimental results from hybrid flat slabs tests carried out recently by the authors [9], as well as results from tests on conventional RC flat slabs [22].

2.1 Modelling Procedures

Three-dimensional (3D) models were constructed in ABAQUS [25] to represent the hybrid members. Using symmetry, only a quarter of the slab assemblage was modelled, as indicated in Figure 1a,b. Use was made of 8-noded brick elements (C3D8R) for concrete and steel profiles, in conjunction with 3D wire elements (T3D2) for the longitudinal reinforcement. For RC specimens, the concrete and reinforcement steel was modelled similarly to the hybrid members. The contact between the steel profile and the concrete body was represented using an exponential decay friction law. In all models, the reinforcement was embedded in the concrete body and assigned with full bond conditions. The support and load application plates were 3D solid regions assigned with elastic steel material properties. Member displacements were applied to reference points that are connected with beam multi-point constraints to reaction plates. Similarly, pinned boundary conditions were assigned to a reference point that was tied to the loading plates. Symmetric boundary conditions were incorporated. The Newton-Raphson approach was adopted for the numerical integration procedure.

The concrete damaged plasticity model (CDP) was used to represent the triaxial behaviour of concrete. This is an isotropic scalar damage model that uses a potential yield surface in the effective stress space (σ) derived from a combined Drucker–Prager and Rankine representation. The plastic yield surface is defined by uniaxial stress-strain σ - ϵ relationships in compression and tension and related scalar damage ratios, the ratio between the bi-axial compressive to uniaxial compressive strength ($f_{b0}/f_c = 1.16$) and a factor $K_c = 2/3$ that controls the shape of the deviatoric plane that represents the ratio of the second stress invariant on the tensile meridian to the one of the compressive meridian. In this model, the plastic volume expansion is not proportional to the increase in stresses (i.e. non-associative flow rule), described by the dilation angle of the material ϕ , and flow potential eccentricity $\epsilon=0.1$. Similarly to previous numerical simulations for one-way hybrid member [12], a plastic stiffness degradation scheme, typical for coupled damage-plastic concrete constitutive models [26,27] was adopted. In the pre-peak region, no degradation occurs and the plastic strains are equal to the inelastic strains. In the post-peak region, the stiffness reduction enables the development of irreversible plastic strains that are directly proportional to the stress decrease.

In this investigation, the compressive stress-strain behaviour was defined using the Eurocode 2 [28] recommendations for non-linear structural analysis. The σ - ε relationship was defined by the concrete compressive strength f_c assessed on cylinder specimens on the day of testing. The elastic concrete modulus E_c and crushing strain ε_{cl} were determined as a function of f_c . The ultimate compressive strain considered is $\varepsilon_{cl} = 0.0035$. Close inspection of several constitutive models, including models that account for post-peak compressive behaviour as a function of the crushing energy G_c of the concrete, showed that the deformational response of some of the validated members with brittle failures was characterised by unrealistic ductile behaviour. To avoid such predictions, it was considered that beyond ε_{cl} the compression stress drops to zero (Figure 1c). In tension, linear elastic behaviour was accounted for up to cracking, followed by a non-linear tension stiffening law [29], in which the tensile strength of concrete f_{ct} was assessed as a function of the f_c [28]. The numerical input was converted into inelastic cracking strain $\varepsilon_{ct,i}$ using the concept of equivalent crack length in which the crack displacement w_i up to $w_{max}=160 \mu\text{m}$, is divided by the characteristic length of the element l_{ch} . The characteristic length of a 3D element is the cubic root of the volume of the mesh element V_e . Both structural and reinforcement steels were modelled with bi-linear elasto-plastic material properties without hardening (Figure 1d).

Specimen HS13-00 from the hybrid flat slab series was selected to simulate numerical models consisting of hybrid members [9], and Specimen PG1 was chosen to validate numerical aspects for conventional RC flat slabs [22]. The parameters varied in the sensitivity analysis were the dilation angle φ , mesh size, and the uniaxial tension material post-peak representation. The steel-concrete interfacial friction coefficient μ was also examined in the case of hybrid members. After achieving good agreement with test results from HS13-00 and PG1, the parameters were applied to the remaining members and compared in terms of load-displacement response V - δ , strain levels ε in constituent elements, and failure modes. In this section, numerical results are reported only for HS13-00 and PG1 which were used for calibration. Comparative assessments for all other hybrid and conventional RC members are given in detail in Sections 2.2.3 and 2.3, respectively.

In terms of mesh density, the results were largely independent of the size l_m for both hybrid (Figure 2a) and conventional RC (Figure 2b) configurations, (when l_m varies from $h/5$ to $h/10$, where h is the flat slab thickness). The use of a fracture dependent post-peak tension behaviour for concrete allowed tension damage localization as a function of the chosen mesh

size. Close inspection of members with low amounts of longitudinal reinforcement ρ_l , provided with coarser mesh ($l_m=h/5$), showed unrealistic rigid behaviour in the cracked regime, primarily due to the delayed cracking as a result of poor propagation of tension damage in the continuum. Intermediate values for mesh sizes, around $l_m=h/7$, were chosen as a reference for further validation and parametric assessment. In addition to this, the influence of the accounted stress transfer through cracked interfaces was investigated by accounting for three post-cracking strain distributions (Figure 2c). Non-linear representation of the post-peak tension behaviour was chosen as opposed to linear and bi-linear laws, since the latter two produced stiffer numerical response, particularly for members with low amounts of ρ_l .

In CDP, the material dilation angle φ is used to represent the stress increase at high confining pressures in the normal-shear stress p - q plane. In RC flat slabs, concrete in the column region is under bi-axial or tri-axial confinement. Hence, for these cases, parameters such as φ control the numerical predictions. Figure 2d,e illustrate the numerical response with φ varying from 10° to 55° . As already noted in other studies on RC flat slabs [17,19], the most effective response is given for $\varphi = 40^\circ$, whereas for the hybrid flat slabs for $\varphi = 49^\circ$. It shows that for hybrid members, the presence of the shear-head produces higher confinement in the concrete at the connection region to the steel column. The steel-concrete interface in hybrid members is also subjected to friction. As mentioned above, the contact between the steel profile and the concrete body is modelled using an exponential decay law with friction coefficients varying between $\mu=0.2$ - 0.6 [30,31]. In the sensitivity analysis depicted in Figure 2f, μ was varied from low friction (0.2) to relatively high friction (0.6). For $\mu = 0.2$, the load-strain response shows softer behaviour, activated by an earlier slip, in comparison to cases with $\mu = 0.4$ - 0.6 . Based on the comparative results shown in Figure 2f, $\mu = 0.4$ was used in all the analysis cases described in the validation studies and parametric assessments.

2.2 Hybrid Slabs with Shear-Heads

2.2.1 Test Set-up and Specimen Details

More detailed validation of the numerical approaches described above are carried out herein against four large scale tests carried out by the authors on hybrid members with cruciform H-shaped shear-head systems fully embedded into RC flat slabs and welded to steel column stubs [9] (Figure 3a). The nominal thickness of the flat slabs was $h = 225$ mm, whereas the plan dimensions were $2.2 \text{ m} \times 2.2 \text{ m}$. The specimens consisted of a closed section steel

column stub that had four directly welded shear heads which were fully embedded in the RC flat slab (Figure 3b,c). The adopted column size was HEB240 in all specimens, with two 20 mm plates welded on the free edges of the profile, resulting in a closed box section (240 mm \times 280 mm). Load transfer plates with 30 mm thickness were welded to the top and bottom of the column. Penetration of the longitudinal reinforcement through the column was allowed by 25 mm drilled gaps. European section HEB 100 shear-heads, with embedded length of $l_v = 370$ mm, were welded symmetrically to the four faces of the column. Two of the members were provided with continuity plates around the column. Eight support plates of 40 mm thickness and 180 mm diameter were tied through 32 mm bolts located at the slab reaction radius ($r_s = 964$ mm from the centre of the column). The top flexural reinforcement ratio ρ_l varied from 0.33% to 1.37%, and the concrete compressive strength on the day of testing varied from 29.0 to 39.2 MPa. A summary of the specimen details and material properties is given in Table 1.

2.2.2 Experimental Results

The main experimental results for the four specimens described above are given in Figure 4 [9]. Specimens HS13-00 and HS13-C0, without shear reinforcement and with relatively high longitudinal reinforcement ($\rho_l = 1.37\%$) exhibited similar behaviour throughout the loading process reaching an ultimate strength of $V_{test} = 1005$ kN and $V_{test} = 991$ kN, respectively. Specimens with intermediate (HS07-C0) and low (HS03-00) ρ_l had lower ultimate strengths. The specimen with the lowest conventional ρ_l failed at $V_{test} = 582$ kN, whereas Specimen HS07-C0 failed at $V_{test} = 880$ kN. Similar behaviour was observed for all hybrid members at early loading stages characterised by flexural cracking. Crack widths and patterns depended on the amount of bending reinforcement. The general in-plane crack path was characterised by orthogonal and diagonal lines, similar to typical yield-line patterns. Wider cracks were observed in the region of the shear-head flanges for the weak axis rotation. This led to a slight non-symmetric rotational behaviour, primarily due to the geometry of the column.

No plasticity was recorded by the strain gauges located on the longitudinal reinforcement as well as the flanges and webs of the shear-heads in Specimens HS13-00 and HS13-C0. Specimen HS07-C0 exhibited yield strains on the top flange at the column face near the ultimate load. Specimen HS03-00 showed clear ductile behaviour due to yielding of the reinforcement. For HS13-00, HS13-C0 and HS07-C0, the failure, attributed to punching shear, occurred due to the development of a punching shear crack that initiated in the hybrid

sector, illustrated in Figure 3c, at the concrete-to-composite interface (about $1.0d$ from the tip of the shear-head) due to the force transfer through struts supported on the bottom flange of the shear-head. Furthermore, the failure propagated towards the RC sector producing an asymmetric tri-dimensional surface bounded by an octagonal pattern on the top face and a rectangular pattern on the bottom face of the slab [9]. Specimen HS03-00 exhibited a ductile behaviour of the flexural reinforcement, yet failure eventually occurred due to the dislocation of a punching cone, and was thus characterised as a failure mode similar to ‘flexural punching’ in conventional RC flat slabs.

2.2.3 Comparative Results

Figure 4a shows the predicted numerical response for the two hybrid members without continuity plates (HS13-00 and HS03-00). They represent the two extreme cases of the studied configuration in which the reinforcement ratio ρ_l varied from 0.33% to 1.38%. This led to two distinct failure modes. Specimen HS13-00 was characterised by brittle failure that is correctly predicted by the numerical model. Both the elastic and cracked stiffness show good agreement with the tests. The predicted behaviour of the specimens with continuity plates (HS13-C0 and HS07-C0) was also in good agreement with the tests (Figure 4b). Although the cracked stiffness of Specimen HS07-C0 shows a slightly more flexible response and marginally higher displacement at ultimate, the discrepancy in strength is within 2%, and the failure mode is captured accurately. The response and strength were also faithfully predicted for Specimen HS13-C0 as indicated in Figure 4b and Table 1.

It is also noteworthy that the predicted ultimate strength $V_{u,num}$ of HS13-00 was only 1% lower than the test strength V_{test} , and the displacement at failure was within a discrepancy of 3%. In addition, the predicted reinforcement strains were nearly identical to those recorded by strain gauges in the test (Figure 4c). They both show that elastic reinforcement behaviour was maintained, both at the column face (LC) and at the composite-to-concrete interface (LI), up to failure. Similarly, the overall behaviour of HS03-00, with relatively low longitudinal reinforcement, was accurately predicted up to the peak strength showing identical elastic and cracked stiffness to those from the test. Beyond the peak strength, the numerical model was unable to predict the softening behaviour due to its intrinsic continuum approach. However the numerical results were only within a 3% difference from the test, and the failure mode was well predicted. Figure 4d shows that at the column face (LC) the reinforcement reached yield strains at load values around 485 kN, whereas at the composite-to-concrete interface

(LI) they remained within elastic limits. The tension yield flag parameter, that illustrates the mesh regions in which the cracking strain is reached, depicts patterns that correspond to the cross-sectional cracks obtained in the tests (Figure 5). All numerical models showed yield regions that resemble the inclined crack patterns from the tests, with the model of HS03-00 exhibiting the highest degradation.

2.3 Conventional RC Flat Slabs

To provide wider validation of the modelling procedures and additional confidence prior to conducting parametric studies, numerical simulations were also carried out tests on conventional RC flat slabs [22]. Similarly to the hybrid tests described in Section 2.2, these members were provided with flexural reinforcement ratios ρ_l that vary from relatively low (0.25%) to comparatively high (1.5%) values. The main aim of the tests was to assess the influence of ρ_l and specimen size on the punching shear strength of conventional RC flat slabs. Double size and half scale members to the Reference Specimen (PG1) were reported. The plan dimensions of PG1 were 3 m \times 3 m, whereas its thickness was $h = 250$ mm. The double size specimen (PG3) was 6 m \times 6 m in plan and 500 mm thick. Half scale specimens (PG6-PG9) were only 1.5 m \times 1.5 m in plan with thickness $h = 150$ mm. The load arrangement and boundary conditions were similar to the hybrid members described in the previous section. The specimen details and material parameters of the specimens considered herein are summarised in Table 2.

For specimens with high ρ_l (PG1, PG6, PG7, PG11), failure occurred in punching due to the dislocation of a conical body out of the slab. In two cases, some reinforcement yielded over the column. None of these specimens reached their plastic regime. On the other hand, specimens with low ρ_l (PG2b, PG4, PG5, PG8, PG9, PG10) showed clear ductile behaviour with a visible plastic plateau. Despite the low ρ_l , the double scale specimen PG3, failed in punching shear at a lower load than its flexural strength [22]. Identical failure modes were obtained through the numerical models adopting the procedures described above. In most cases, both the elastic and cracked stiffness were accurately predicted, and the ultimate strength was well captured (Table 2 and Figure 6a-f). The predicted strength of several members with low $\rho_l = 0.25\%$ (e.g. PG2b, PG4) was slightly overestimated by about 6% on average primarily due to the late cracking in the numerical model in comparison with the tests (Figure 6a,b). On the other hand, the ultimate strength of member PG5, also provided with low $\rho_l = 0.33\%$, was underestimated with an average $V_{test}/V_{u,num}=1.04$ (Figure 6c).

Additionally, the cracking load of the double-size specimen was underestimated by about 30% leading to a premature development of inelasticity compared to the test. However, there is close agreement between the numerical and test results in terms of the cracked stiffness and the ultimate strength (Figure 6d). Specimens with high ρ_l (e.g. PG1 and PG6) showed faithful strength predictions with a discrepancy of around 3% from the test values (Figure 6e,f),

Overall, the load-displacement (V - δ) curves in Figure 4a,b and Figure 6, as well as the crack patterns in Figure 5 and strain levels in Figures 4c,d, enabled a direct assessment of the nonlinear numerical models described in Sections 2.2.3 and 2.3. The strength, deformational response and failure modes obtained from the numerical simulations were generally in very good agreement with the corresponding test measurements. Having gained confidence in the modelling procedures through the two sets of validations described above, detailed parametric studies were carried out, as described in the following section, in order to provide further insights into the behaviour of hybrid slabs with shear heads as well as to support analytical and design approaches.

3. Parametric Assessments

A total of 92 models were constructed, using the numerical procedures described above, in which steel columns were connected to RC flat slabs by means of full-embedded shear-heads. The parametric investigations described in this section are undertaken to provide detailed insights into the physical behaviour for a wide range of hybrid configurations outside of the existing test database [6-9]. The experimental study reported by the authors elsewhere [9] focused on one specific RC slab geometry ($h=225$ mm) in which the reinforcement ratio ρ_l (i.e. ρ_l 0.33%, 0.75%, 1.38%) and the presence of the continuity plate around the column were directly investigated [9]. On the other hand, existing investigations [6-7], studied two primary flat slab configurations with similar thicknesses (e.g. $h=200$ mm and $h=300$ mm [6,7]) and varying shear-head embedded lengths. Also, a single monotonic test with a slab thickness of $h=155$ mm is reported elsewhere [8]. As observed, these experimental studies offer a limited range of test configurations. The analytical models validated against such limited number of tests show reliability only for applications within the tested ranges. Hence, parametric investigations with the variation of main structural parameters outside of the tests range are required to enhance the applicability of these analytical models. Consequently, the numerical results obtained from the numerical parametric investigations described in this

section enable a direct assessment of the behaviour of hybrid flat slab members in terms of strength and deformation characteristics and provide wider validation for practical application of the analytical models.

Considering the numerical model for Specimen HS13-00 as a reference (see Table 1 and Figure 4a,c, the parametric assessments (summarised in Table 3) may be grouped into five main studies in which the following key parameters were investigated:

- *Shear-head embedment length-to-depth ratio ($l_v/h_v=0.5-5.0$):* in each case, the reinforcement ratio ρ_l was varied from 0.33% to 2.20%, whereas the effective depth d , slab radius r_s , concrete strength f_c and shear-head section size ($h_v \times b_v = 100 \times 100$ mm, from a HEB100 profile), were maintained constant
- *Slab radius ($r_s/d=5.44-8.47$):* in conjunction with $\rho_l=0.33\%-2.20\%$, and constant l_v , d , f_c , r_s/d , and $h_v \times b_v$
- *Slab bending effective depth ($d=140-330$ mm):* in conjunction with $\rho_l=0.33\%-2.20\%$ with constant l_v/h_v , f_c , r_s , and $h_v \times b_v$
- *Shear-head section size ($h_v \times b_v = 60 \times 60-120 \times 120$ mm):* for $l_v=370$ mm and constant f_c , r_s , d
- *Concrete strength from $f_c = 29 - 80$ MPa and $\rho_l = 0.33\% - 2.20\%$* for constant l_v/h_v , d , r_s and shear-head section size

The results of the parametric studies are plotted in terms of rotational response ($V-\psi$) in which the load V was normalised against the control perimeter b_0 as a function of the critical length l_0 , shear effective depth d_0 and concrete strength f_c , as described by Equation 1a-c and illustrated in Figure 7a,b. A detailed analysis on stress fields [9] showed that b_0 , required for punching shear assessments in the case of hybrid slabs provided with shear-heads, can be expressed in terms of l_0 . As shown in Figure 7b, b_0 is defined for each shear-head by an arc length with a radius equal to the in-plane strut projection d_0 plus two critical lengths l_0 . For short shear-heads, the diagonal lines of the control perimeter extending from the shear-head tip regions could join, resulting in a closed shape. It can be evaluated using Equation (1a) as the minimum of the above two conditions.

Besides the obtained $V-\psi$, Figures 8,10,11 assess failure criteria (FC) for punching shear in RC flat slabs [23], which were also extended to hybrid slabs [9] (Equation 2), and provide key observations on member behaviour. These include envelopes of the loads corresponding to yielding in the steel reinforcing materials, namely: longitudinal reinforcement (RY), flange

of shear-head (FY), web of shear-head (WY) and the ultimate envelope (U). In the case of RY, the points on the graph correspond to the initiation of yielding in one wire element in the analysis. For FY and WY, they correspond to the case in which yielding spreads in a band (i.e. at least two mesh elements for FY, typically at the edges of the flanges; or a band of mesh elements in which WY occurs from the top flange to bottom flange).

$$b_0 = \min(\pi d_0 + 8l_0, \pi d_0 + 4[l_0 + (b_c - b_v)/2]\sqrt{2}) \quad (1a)$$

$$l_0 = l_v + d_0 / 2 \geq h_v \quad (1b)$$

$$d_0 = d - d_{vfb} - t_f / 2 \quad (1c)$$

$$k_\psi = 0.75 / \left[1 + 15 \cdot \psi \cdot d / (d_{g0} + d_g) \right] \quad (2)$$

The results of the parametric studies are grouped below in observations regarding the influence of the shear-head embedment length, shear-head section size and slab thickness, and the concrete strength. These results are then used in Section 4 for practical analytical and design considerations.

3.1 Shear-Head Embedment Length

Figures 8a-e illustrate the rotational response $V-\psi$ from numerical models in which the embedment length l_v was varied against the flexural reinforcement ratio ρ_l . For low to intermediate reinforcement ratios ($\rho_l = 0.33\text{-}0.78\%$) combined with short shear-heads ($l_v/h_v=0.5\text{-}1.0$; $l_v/r_s=0.05\text{-}0.10$), yielding of the longitudinal reinforcement bars (RY) governs the behaviour. As l_v increases, inelastic strains develop at the shear-head flange edges (FY). For $l_v/h_v=2.3$ ($l_v/r_s=0.24$) and $\rho_l=0.78\%$, (RY) is triggered before (FY). For intermediate to high reinforcement ratios ($\rho_l=1.38\text{-}2.20\%$), flexural yielding (FY) is arrested and failure is governed by crushing at the composite-to-concrete interface combined with yielding of the shear-head flange in compression (for $l_v=0.5\text{-}1.0$; $l_v/r_s=0.05\text{-}0.10$) or by local yielding of tension flanges and eventual crushing at the interface (for $l_v=2.3\text{-}5.0$; $l_v/r_s=0.24\text{-}0.51$).

As depicted in Figures 8d,f, an increase in slab radius from $r_s/d=5.44$ ($r_s=964$ mm) to $r_s/d=8.47$ ($r_s=1500$ mm), for constant $l_v=370$ mm ($l_v/r_s=0.38$ and $l_v/r_s=0.25$), leads to an increase in rotations ψ at ultimate, which indicates a more flexible slab behaviour. In the latter case, inelastic strains develop in the flanges of the shear-head (FY) at lower normalised

strengths due to higher bending moment carried out by the slab strips which contain the shear-heads. Although (FY) governed the behaviour for low ρ_l , punching occurred at ultimate for cases with intermediate to high ρ_l .

As suggested by the position of (FY) envelopes in Figures 8a-e, an enhancement of the composite action is produced with an increase in l_v , primarily due to the higher contact surface between the shear-heads and surrounding concrete. Although in some cases yielding of the shear-head flanges (RY) occurs, with its web remaining within the elastic regime, punching shear governed the behaviour at ultimate. This is illustrated by the ultimate envelopes (U) which are in proximity to the punching shear failure criterion (FC). It is also worth noting that the stiffness degradation patterns in Figures 9a-d are characterised by inclined damage zones which correspond to punching shear failure surfaces.

3.2 Shear-Head Section Size and Slab Thickness

The influence of the ratio between shear-head section size and slab thickness was examined in three parametric studies. Initially, the slab effective depth d was varied from 140 to 330 mm for two embedment length ratios $l_v/h_v = 1.0$ and $l_v/h_v = 3.7$, and each of the two ratios was also used for four longitudinal reinforcement ratios ρ_l between 0.33 and 2.20 %. In addition, the shear-head cross-section was varied from H60 to HEB120 for ρ_l between 0.33 and 2.20 %, whereas the l_v was 370 mm ($l_v/h_v = 0.62-0.31$; $l_v/r_s = 0.38$). For compactness, only the results of six of these variations are depicted in Figure 10a-f.

Similar to other observations made before, members with low $\rho_l=0.33\%$ developed inelastic strains in the longitudinal bars (RY). Apart from slabs with $d=300$ mm, in which yielding at the top edges of flanges was observed, members with short shear-heads ($l_v/h_v=1.0$) exhibited elastic shear-head behaviour with failure triggered by crushing at the composite-to-concrete interface. This can be noted from the comparative assessment of the ultimate envelope (U) and the punching shear criterion (FC) in Figures 10a,b and 8b. For longer shear-heads ($l_v/h_v=3.7$; $l_v/r_s=0.38$) and rather thin slabs ($d=140$ and 177), the behaviour is governed by punching at ultimate with inelastic strains occurring in the flexural reinforcement (RY) or shear-head flanges (FY), depending on the slab configuration (Figures 10b and 8d).

As the slab thickness increases ($d=230-330$ mm) the ultimate envelopes (U) show trends below (FC), which identify failure mechanisms different than those described above (Figure

10d). For these cases, failure was triggered by yielding in the web of the shear-head (WY), which resulted in lower normalised member capacities than those from (FC). Similarly, for $d=177$ mm and the smallest investigated shear-head section size (H60), failure was also triggered by web yielding (WY) as illustrated in Figure 10e. As a result, for small $h_v/d < 0.43$ and $l_v/r_s=0.38$, a rather undesirable behaviour of the shear-head assemblage is observed due to the lower stiffness ratio between the shear-head and surrounding concrete. On the other hand, as the shear-head section depth increases ($h_v \geq 80$ mm), the behaviour at ultimate reverts to typical crushing at the composite-to-concrete interface (Figure 10d). Figure 11 illustrates the damage tension kinematics of a case in which web yielding developed. The numerical results show that web yielding was produced by a sudden slip (Figure 11a) of the shear-head from the embedding concrete which led to a premature punching shear failure (Figure 11b).

3.3 Concrete Strength

The influence of the concrete strength on hybrid slab behaviour was considered by varying the concrete constitutive laws in compression and tension for compressive peak strengths of $f_c = 29, 40, 60$ and 80 MPa as described in Section 2.1. Figure 12 depicts the normalised V against rotation ψ for cases in which f_c was varied against ρ_l . For compactness, only the extreme curves for each ρ_l are presented. In the normalised plots, the upper curves represent predictions for $f_c=29$ MPa, whereas the lower curves are numerical results for $f_c=80$ MPa. Additionally, ultimate envelopes (U) are plotted for each set of ρ_l and f_c , and show that member flexibility increases with the decrease in ρ_l combined with higher effectiveness when low f_c is used. Cases with normalised ultimate strengths below (FC), with intermediate and high ρ_l (1.38–2.20%), showed failures generally triggered by shear-head web yielding (WY).

The results of the parametric studies identified three modes of failure as a function of the interaction between the shear-head and surrounding concrete: punching shear due to crushing with or without yielding of the reinforcement or top flange of the shear-head – referred to as controlled failure (A); failure due to yielding of the compression flange due to inefficient strut support and crushing of the strut (B) and; failure due to yielding of the shear-head flange and web leading to uncontrolled slip (C). These observations, with the complementary key findings from the numerical investigations described in this study, in conjunction with those from the test results described in Section 2.2.2, enable the validation of analytical models for a wide range of hybrid slab systems. The V - ψ responses and ultimate strength predictions are used for the modification and validation of a recently proposed bi-linear rotational V - ψ model

[9]. These predictions are also used for the definition of key shear-head related parameters which are required for the design for punching shear and flexure of hybrid systems with shear-heads, with focus on the specification of the shear-head embedment length and section size.

4. Analytical Models and Design Considerations

4.1 Load-Rotation Response

An axisymmetric rotational model that considers that relatively stiff shear-heads in conjunction with the continuity reinforcement transfer the entire load from the steel assemblage to the RC flat slab, was proposed previously [9]. The model is based on compatible yield mechanisms that divide the in-plane layout into RC sectors and hybrid sectors, with shear-heads embedded in the hybrid sectors (Figure 3c). In each sector, corresponding constitutive, compatibility and equilibrium relationships apply. A more simplified bi-linear model, derived from the axisymmetric model, was also proposed for assessing the V - ψ response. The model, initially developed from the tests described in Section 2.2, is employed in this study and appraised against the numerical simulations described in Section 3. Since the slab flexibility is the governing factor for assessments of the flat slab punching shear strength [9,23], the prediction of the load-rotation V - ψ response must have a significant degree of reliability. Hence, a focal point in the numerical parametric investigations described in Section 3 was the prediction of the rotational response V - ψ for configurations outside of the tested ranges. Consequently, the λ_ψ factor in Equation (3a) that accounts for slab flexibility through the shear-head embedment length l_v and reinforcement ratio ρ_l is represented in this paper in an improved form which is validated against the results from the parametric assessments in Section 4. The remaining equations required to assess the V - ψ response have the same form as proposed previously [9].

The rotation ψ of the hybrid member, determined using Equation (3a), depends on the section utilisation factor V_i/V_{flex} , in which V_{flex} is the flexural strength of the slab and V_i is the shear action. Other parameters include the slab radius r_s , yield strength f_{ys} and elastic modulus E_s of the longitudinal reinforcement, slab effective depth d , and a factor λ_ψ (Equation 3b) that accounts for slab flexibility through the shear-head embedment length l_v and reinforcement ratio ρ_l . The flexural strength V_{flex} given by Equation (4a) is a function of η (Equation 4b)

which accounts for the in-plane distribution of the sectors, the plastic moments of the hybrid sectors m_{Rk} (Equation 5a,b) and the concrete sectors m_{Rc} (Equation 5c,d), and the slab configuration (l_v , r_s , r_e , r_c). The plastic moments per unit width in Equation 5 may be determined from assumptions of linear strain compatibility in the cross-section, in which yielding occurs first in the tension reinforcement.

$$\psi = \lambda_\psi \frac{r_s}{d} \frac{f_{ys}}{E_s} \left(\frac{V_i}{V_{flex}} \right)^{3/2} \quad (3a)$$

$$\lambda_\psi = \frac{2}{3} \left(100 \rho_l \frac{r_s}{l_v} \right)^{1/3} \quad (3b)$$

$$V_{flex} = \pi \left(\eta \frac{l_v}{r_s} m_{Rk} + \left(2 - \eta \frac{l_v}{r_s} \right) m_{Rc} \right) \frac{r_e}{r_s - r_c} \quad (4a)$$

$$\eta = 8 \sin^{-1} (0.5 b_v / r_c) \quad (4b)$$

$$m_{Rk} = f_{ys} \left\{ A_s \left(d - \frac{c_k}{2} \right) + \Sigma \left[A_{vij} \left\langle (d_{vij} - c_k) (d_{vij} - c_k / 2) \right\rangle \right] / (d - c_k) \right\} \quad (5a)$$

$$c_k = \frac{f_{ys} \left(A_s + A_{vft} \left\langle \frac{d_{vft} - c_{k,0}}{d - c_{k,0}} \right\rangle + A_{vw} \left\langle \frac{d_{vw} - c_{k,0}}{d - c_{k,0}} \right\rangle + A_{vfb} \left\langle \frac{d_{vfb} - c_{k,0}}{d - c_{k,0}} \right\rangle \right)}{\lambda f_c b_c} \quad (5b)$$

$$m_{Rc} = f_{ys} A_s \left(d - \frac{c_c}{2} \right) \quad (5c)$$

$$c_c = \frac{f_{ys} A_s}{\lambda f_c b_c} \quad (5d)$$

$$\text{where } \langle x \rangle : (< 0 = 0; \geq 0 = x)$$

Figure 13 illustrates a comparison between the V - ψ response from numerical simulations with the predicted response from Equations (3-5). Considering the limitations of a bi-linear approach, the model predicts reasonably well the stiffness response of hybrid members for all reinforcement ratios ρ_l and for practical ratios of embedment length l_v/h_v . The predicted V_{flex} , attained in members with low amounts of $\rho_l = 0.3\%$, is in good agreement with all numerical results and test results of Specimen HS03-00. The analytical results show consistency with

numerical results since the full flexural capacity is reached only for models with very low amounts of ρ_l .

4.2 Shear-Head Properties

4.2.1 Embedment length

The experimental results described in Section 2.2 showed that the critical section in hybrid slabs is located within the critical shear region at the composite-to-concrete interface, and depends on the governing strut support location and its inclination, as shown in Figure 7. The numerical simulations in Section 2 and 3, as partly illustrated in Figure 9, also show that in all cases the critical shear crack originated from the bottom flange of the shear-head.

The numerical and experimental results support the assumption of shear transfer through inclined struts, and the definition of a critical length l_0 Equation (1b) as a function of the embedment length l_v and shear effective depth d_0 Equation (1c). The embedment length l_v of a shear-head may be determined from the assumption that the critical section is situated at the composite-to-concrete interface l_0 , which results from the length of the control perimeter $b_{0,req}$ as a function of the shear action V_i Equation (6a) (k_ψ assessed with Equation (2)). Consequently, the critical length $l_{0,req}$ can be evaluated with Equation (6b) and the required embedment length $l_{v,req}$ using Equation (6c).

$$b_{0,req} \geq V_i / (k_\psi \sqrt{f_c} d_0) \quad (6a)$$

$$l_{0,req} = \max \left[(b_{0,req} - \pi d_0) / 8; (b_{0,req} - \pi d - 2(b_c - b_v) \sqrt{2}) / (4 \sqrt{2}) \right] \quad (6b)$$

$$l_{v,req} = l_{0,req} - d_0 / 2 \geq 2h_v \quad (6c)$$

Figure 14 illustrates the relationship between the shear-head characteristic dimensions in relation with predictions of the shear-head length $l_{v,req}$ by Equation (6c) corresponding to the imposed l_v in the numerical models and experiments. It may be observed that relatively long shear-heads, with relatively small depth h_v compared to slab thickness, are located in the bottom left corner of the figure. This shows that the imposed h_v and b_v are much smaller than required for a smooth force transfer. These sizes would also be ineffective since web shear failure may develop.

On the other hand, short shear-heads, in the range of $l_v/h_v \leq 1.0$, are unable to support the force-transferring struts, which may lead to compression yielding of the bottom flange and slip. These members are depicted in the top right corner of Figure 14 and show that the imposed l_v in the parametric studies are below the required $l_{v,req}$. Although, in these cases the behaviour at ultimate is controlled and the ultimate envelopes (U) in Figures 8 and 10 are in the range of the failure criterion (FC), the beneficial effect of the shear-head is limited and the behaviour becomes similar to a RC member.

For members with intermediate l_v and intermediate shear-head depths ($h_v/d \geq 0.43$), controlled failures are generally obtained. Depending on the flexural reinforcement ratio ρ_l , one of the steel tension members may yield. Punching shear eventually governs at ultimate in all numerical models for these cases, and the required $l_{v,req}$ is typically in the same range of the imposed l_v . Similar predictions are obtained for the tests described in Section 2.2 and those from the literature [6-8].

4.2.2 Section size

The shear-head section size can be determined by means of linear strain compatibility in the composite cross-section by assuming that the entire shear-head is represented by a single reinforcement bar located at its geometrical centre. The stress in a reinforcement component and its moment contribution to the total resistant moment is a function of the cracked stiffness $I_{k,cr}$ and geometry of the member. The cracked stiffness depends on the geometrical characteristics of the constituent elements of the cross-section. For RC members, the cracked moment of inertia at ultimate varies between 30 and 70% of the un-cracked cross-section.

For hybrid members with shear-heads, examination of the numerical results from the parametric assessments combined with the experimental results described in Section 2.2.2, points to an average ratio of $c_k/d = 0.37$ at ultimate. This leads to a ratio of the shear-head moment of inertia I_v to the cracked moment of inertia of the entire cross-section per unit width of $I_v/I_{k,cr} = 0.25$. The plastic moment of the cross-section can be determined by the contribution of longitudinal reinforcement which yields first, as well as that of the shear-head combined. Considering that the moment action should be limited by the plastic capacity, the shear-head section size may be determined from Equation (7a). For cases without eccentricity, the average moment per unit width acting within the support strip m_i can be determined from the shear action V_i using Equation (7b) [24].

The numerical simulations also identified cases in which yielding of the shear-head web triggered failure (Figure 10d,e). In such situations, the h_v/d ratio was below 0.43. An analysis using the Eurocode 3 [32] relationship for assessing the design plastic shear resistance of the steel insert showed that, in these cases, the shear active area A_{vv} of the shear-head was not sufficient to transfer the force from the slab to the steel column. Accordingly, besides the cross-sectional design in terms of I_v , the shear-head section size should be determined from Equation (8) and accounting for a conservative $h_v/d \geq 0.5$ limit for standard European sections.

Considering that the force is transferred from the slab to the column through struts supported on the bottom flange, the width b_v of the shear-head dictates the cross-sectional strut thickness and, consequently, the amount of force transferred. In order to ensure a smooth transfer, the bottom flange should be relatively stiff in order to avoid failure in compression in the steel insert. The minimum shear-head width b_v may be determined with Equation (9a) based on the assumption that the transferring struts are supported through the entire embedment length l_v , in which crushing strength of the struts may be assessed with (Equation 9b) [24].

$$I_v \geq \frac{m_i}{20} \frac{d}{f_{ys}} \left(1 - \frac{c_k}{d} \right) \quad (7a)$$

$$m_i = V_i / 8 \quad (7b)$$

$$A_{vv} \geq \frac{5}{4} \frac{V_i}{n_v} \frac{\sqrt{3}}{f_{yv}} \quad (8)$$

$$b_v \geq \frac{V_i}{n_v} \frac{1}{\sigma_{c,\max} l_v} \quad (9a)$$

$$\sigma_{c,\max} = 0.55 \left(30 / f_c \right)^{1/3} f_c \quad (9b)$$

The above equations for the design of shear-head section moment of inertia, shear active area and width, offer a set of requirements that should be met in the design procedure of the steel insert. In conjunction with the above expressions, supplementary verifications regarding the moment capacity of the shear-head, as described in the following section, must be carried out.

4.2.3 Moment capacity

Figure 15 illustrates the recorded force distribution per unit width (v/v_{max}) at the top flange of the shear-head as a function of the embedment length l_v . The qualitative distribution (v/v_{max}) of the applied load is based on the strains from numerical simulations and integrated over the cracked cross section. It is observed that the shape of the diagram, which can be divided into two regions, varies with l_v . In all cases, the peak value was recorded within a region of $h_v/4$ from the column face. For short and relatively rigid shear-heads, the distribution takes nearly a triangular form, whereas for flexible steel inserts it shows a non-linear form. In a simplified manner, it can be represented by two rectangular regions delimited by $h_v/4$. Close inspection of the numerical results shows that the average reaction forces in each region vary with shear-head flexibility, and the amount of force transferred through each region can be expressed as a function of the κ factor in Equation (11a). The moment carried by each shear-head $M_{v,i}$ can be expressed as a function of the shear action V_i and the assumed distribution in Figure 15 as depicted by Equation (11b).

$$\kappa = \frac{1}{3} \left(1 - \frac{l_v}{r_s} \right) \quad (11a)$$

$$M_{v,i} = \frac{V_i}{n_v} \left[\kappa \frac{h_v}{8} + (1 - \kappa) \left(\frac{l_v}{2} + \frac{h_v}{8} \right) \right] \quad (11b)$$

In hybrid members with shear-heads, the full plastic capacity of the steel insert is generally not reached since the behaviour is governed by the interaction properties between the shear-head and embedding concrete. The numerical results showed that the shear-head/concrete slip is dependent on the contact surface and, consequently, the embedment length l_v . Hence, the shear-head develops inelastic behaviour, primarily at its top flange, at a fraction of its full plastic capacity (Equation 12a). This can be estimated by accounting for through the λ_m factor which was determined from the numerical simulations in which yielding of the shear-head flange was recorded (Equation 12b).

$$M_{v,i} \leq \lambda_m W_{v,pl} f_{yv} \quad (12a)$$

$$\lambda_m = \lambda_{\psi} \left(\frac{d_0}{r_s} \frac{l_v}{h_v} \right) \quad (12b)$$

Figure 16 shows the predictions of Equation (12a) against the $V_{u,num}/V_{yv,num}$ ratio in which $V_{u,num}$ is the ultimate strength and $V_{yv,num}$ is the force at which yielding developed in the top flange (FY). Values below 1.0 show that no plastic behaviour is predicted ($M_{v,calc}/(\lambda_m M_{v,pl}) < 1.0$), and elastic shear-head behaviour was developed in simulations ($V_{u,num}/V_{yv,num} < 1.0$). It is depicted that the assumed force distribution (Figure 14) in conjunction with the considered moment behaviour (Equations 12a-b) shows good agreement between predictions and numerical results.

4.3 Practical Application

The results from the numerical assessments in conjunction with the test results from Section 2.2.2 enabled the definition of the above expressions for the design of shear-heads in hybrid flat slabs. The required embedment length l_v can be determined from the shear action V_i in the connection region using the modified RC approach [30] for hybrid configurations (Equations 1-6). This has previously been validated on a number of tests [9], and for a wider range of parameters in the numerical studies described in Section 3. The results of the numerical simulations also resulted in expressions for the design of the shear-head cross-section in terms of minimum moment of inertia I_v , shear area A_{vv} and width b_v , as a function of the shear action V_i (Equations 7a-9b).

Figure 17 shows predictions for I_v and A_{vv} plotted against details of some practical shear-head section sizes from European HEB sections embedded in flat slabs with $d=180-330$ mm. It is observed that predictions of Equation (7) show that the required section size increases proportionally with the shear action V_i , apart from the case of $d=180$ mm. Generally, in this situation, the required shear area A_{vv} (Equation 8) governs the shear-head cross-sectional design. In cases in which the effective A_{vv} is smaller than that required, web failure could develop; this type of behaviour was observed in numerical simulations in situations in which the shear-head from European HEB section type had a depth h_v less than $d/2$. Hence, as a general guide, after the assessment of the shear-head section size using Equations (7-9), h_v should be at least $d/2$ for standard European sections, whilst the maximum shear-head depth would be limited by practical aspects including slab thickness, amount of longitudinal reinforcement and concrete cover.

A sensitivity analysis on Equation (6) to assess l_v , along the results from numerical simulations and available tests [6-9] is depicted in Figure 18a. The shear-head section sizes

varied from HEB100 to HEB 140 and for each case the reinforcement ratio ρ_l varied from 0.33% to 2.20% , whilst $h_v/d=0.5$, $r_e/r_s=1.2$, $f_c=30$ MPa, $f_{ys}=500$ MPa, $f_{yv}=355$ were maintained. The predicted l_v/r_s ratios are plotted against the shear action to flexural strength V_i/V_{flex} ratio. Values of $V_i/V_{flex}<1.0$ indicate elastic reinforcement behaviour, whereas values above 1.0 depict situations in which flexural yielding occurs. It is generally observed that the low amounts of ρ_l lead to flexural failures and high shear action V_i requires very long shear-heads with $l_v>r_s$. Members provided with low to intermediate reinforcement (e.g. $\rho_l=0.75\%$) may also reach their flexural strength when small shear-head section sizes are employed (some cases were identified in Figures 8 and 10). Typically, irrespective of l_v , intermediate to high ρ_l produce elastic reinforcement behaviour. Generally, for the same shear action V_i , low ρ_l ratios require shear-heads with higher l_v/r_s in comparison with intermediate and high ρ_l , which may necessitate the use of short to intermediate shear-heads. In addition to this, Figure 13 indicates ineffective behaviour for short shear-heads ($l_v/r_s<0.1$), since they were not able to ensure a smooth force transfer through struts. Also, available tests [6-9] and numerical results from Section 3 for $0.1<l_v/r_s<0.55$ showed effective behaviour and seem generally practical. These observations point to an effective use in design of shear-heads with embedment length-to-slab radius ratios within the range of $l_v/r_s=0.2-0.5$, mainly due to their practicality and stable structural behaviour.

Figure 18b illustrates the predictions of Equations (11) and (12) against V_i/V_{flex} ratio, including the results from the numerical simulations as well as available tests results [6-9]. This figure depicts results from the same sensitivity analysis described in Figure 18a with focus on the shear-head behaviour. It is observed that, considering the predictions of Equations (7-9), irrespective of the shear-head section size, for low amounts of ρ_l , both the reinforcement and shear-head top flange yield, whereas for intermediate and high amounts only the top flange develops inelastic strains. This correlates well with the numerical results and shows that in tests [6-9], the shear-head may have developed inelastic behaviour at the edges of its top flanges, which was not captured by the strain gauges (typically located above the shear-head web). The above remarks show that Equations (11-12) may be used for assessing the onset of yielding of the shear-head top flange. This may be more effective for design since the shear-head full plastic capacity is generally not attained due to characteristic hybrid slip behaviour.

As noted before, the results from the numerical simulations, in conjunction with experimental results described in Section 2.2.2, enabled the development of relationships for the design of shear-heads in RC flat slabs at interior connections to steel columns which may be directly used in the design of such elements. The improved bi-linear rotational model described in Section 4.1, alongside the design expressions for punching shear proposed previously by the authors [9], cover all the key aspects required for the design of hybrid RC flat slab-steel column systems of the form examined in this study. Accounting for the wide range of salient parameters considered in the parametric investigations, the expressions proposed in this paper offer a reliable design approach for hybrid members with shear-heads. The suggested equations for assessing the shear-head characteristics and the ultimate strength of the hybrid members are suitable for direct practical application and implementation in codified procedures.

5. Concluding Remarks

This paper investigated the performance of shear-head systems in hybrid RC flat slabs connected to steel columns. Numerical simulations were carried out, using nonlinear finite element procedures with concrete damage plasticity model, and validated against a series of tests on hybrid steel/concrete flat slabs with shear heads. To provide wider validation of the modelling procedures and additional confidence prior to conducting parametric studies, numerical simulations were also carried out against tests on conventional RC flat slabs. The numerical results showed good agreement with both sets of test results, in terms of ultimate strength as well as deformations and stress levels, indicating the suitability of the adopted modelling procedures including the concrete damage plasticity approach for simulating the response of hybrid and conventional RC flat slab members.

A total of 92 models were considered within the numerical parametric studies in order to obtain detailed insights into the physical behaviour of hybrid slab configurations with shear-heads. This enabled direct assessment of the behaviour both in terms of deformation response and ultimate strength. It also permitted close examination of the main failure modes, with focus on those developing at the composite-to-concrete interface, which are governed by punching shear with or without yielding in the steel. The results of the parametric investigations also provided information on the member kinematics which complement those obtained directly from the tests. Three primary modes of failure were identified as a function

of the interaction between the shear-head and surrounding concrete: (i) punching shear due to crushing with or without yielding of the reinforcement and/or top flange of the shear-head, (ii) failure due to yielding of the compression flange as a result of ineffective support and crushing of the struts, and (iii) failure due to yielding of the shear-head flange and web resulting in uncontrolled slip.

The key findings from the numerical investigations described in this study, in conjunction with available experimental results, enabled improvements to analytical models for hybrid slabs and comparison against a wide range of geometries and constituent parameters beyond those directly examined in tests. The results of numerical simulations combined with results from existing tests show that the critical shear regions occur at the composite-to-concrete interface and that the critical shear crack originates from the bottom flange of the shear-head. The findings support the assumption of a force transfer through inclined struts as well as the definition of a critical length which determines the control perimeter as a function of the shear-head embedment length and shear effective depth. The rotational responses and ultimate strengths obtained from the simulations were also used for the modification and improvement of a simplified bi-linear rotational model.

Importantly, the observations from the numerical simulations permitted the definition of shear-head dependent parameters required for the design of hybrid assemblages incorporating shear-heads, with focus on the design of shear-head embedment length and section size in terms of section moment of inertia, shear active area, shear-head width and depth. Additionally, equations to assess the bending moment at which yielding occurs in the shear-head top flange as a function of its plastic capacity, were also proposed. Finally, practical considerations regarding the design of the shear-head were highlighted. In particular, the results indicated that more effective application can be obtained from intermediate rather than relatively short or long shear-heads provided that the depth is at least half the slab thickness. Accounting for the wide range of salient parameters considered within the parametric investigations, which were subsequently utilised for validation, the analytical expressions proposed in this paper offer a more reliable design approach in comparison with existing approaches. The suggested equations for determining the required shear-head properties and predicting the ultimate strength of the embedding hybrid members are suitable for direct practical application and implementation in codified procedures.

Acknowledgements

The authors acknowledge the financial support of the Research Fund for Coal and Steel of the European Community within the project SMARTCOCO: “Smart Composite Components – Concrete Structures Reinforced by Steel Profiles”, Grant No. RFSR-CT-2012-00031, for the tests described in this paper. The many useful discussions with all the collaborators within the project, particularly Professors André Plumier and Hervé Degée, are also gratefully acknowledged.

References

- [1] Corley WG, Hawkins NM, Shearhead Reinforcement for Slabs. ACI Journal Proceedings 1968;70(11):811-824.
- [2] Piel W, Hanswille G, Composite shear head systems for improved punching shear resistance of flat slabs, Composite Construction in Steel and Concrete V, 2006: 226-235.
- [3] Tuchs Schmid AG. Tuchs Schmid-WALM Dokumentation – Stützenkopfverstärkung - Optimale Krafteinleitung auf tragende Stützen. Frauenfeld (Switzerland): Tuchs Schmid AG, 2007
- [4] Huber K, inventor; Geilinger .AG, assignee. Method of manufacturing a building. European patent EP0128994. 1984 December 27
- [5] Chana, P. S. and Birjandi, F. K., Design guidance on structural steel shearheads in concrete (shearhead development tests). Report. Department of the Environment, Imperial College London UK; 1996 July, CRIC Report No. CRIC95/001/F
- [6] Lee CH, Kim JW, Song JG, Punching shear strength and post-punching behaviour of CFT column to RC flat plate connections. Journal of Constructional Steel Research, 2008;64(4):418–428
- [7] Kim JW, Lee CH, Kang THK, Shearhead reinforcement for concrete slab to concrete-filled tube column connections. ACI Structural Journal, 2014;111(3):629-638
- [8] Eder MA, Vollum RL, Elghazouli AY, Inelastic behaviour of tubular column-to-flat slab connections. Journal of Constructional Steel Research, 2011;67(7):1164–1173
- [9] Bompa DV, Elghazouli AY. Structural performance of RC flat slabs connected to steel columns with shear heads. Eng Struct 2016; 117:161–183.
- [10] Bompa DV, Elghazouli AY. Force transfer mechanisms between steel columns and reinforced concrete beams by means of shear keys. In: Proceedings of Eurosteel 2014, 7th International Conference on Steel and Composite Structures 2014 September 10-12; Naples, Italy; 2014. Session 6, Paper No 03-476
- [11] Bompa DV, Elghazouli AY. Ultimate shear behaviour of hybrid reinforced concrete beam-to-steel column assemblages, Eng. Struct 2015; 101:318–336.
- [12] Moharram MI, Bompa DV, Elghazouli AY. Experimental and numerical assessment of mixed RC beam and steel column systems. Journal of Constructional Steel Research. 2017 Apr 30;131:51-67.
- [13] Hallgren M, Bjerke M. Non-linear finite element analyses of punching shear failure of column footings. Cement and Concrete Composites. 2002 Dec 31;24(6):491-6.
- [14] Mamede NF, Ramos AP, Faria DM. Experimental and parametric 3D nonlinear finite element analysis on punching of flat slabs with orthogonal reinforcement. Eng. Struct 2013; 48:442-57.
- [15] Shu J, Plos M, Zandi K, Johansson M, Nilenius F. Prediction of punching behaviour of RC slabs using continuum non-linear FE analysis. Engineering Structures. 2016 Oct 15;125:15-25.

- [16] Soares LF, Vollum RL. Influence of continuity on punching resistance at edge columns. Magazine of Concrete Research; 2016;68(23):1225-1239.
- [17] Genikomsou AS, Polak MA. Finite element analysis of punching shear of concrete slabs using damaged plasticity model in ABAQUS. Engineering Structures 2015;98:38-48.
- [18] Wörle P. Enhanced shear punching capacity by the use of post installed concrete screws. Engineering Structures 2014; 60:41-51.
- [19] Bompa DV, Onet T. Punching shear strength of RC flat slabs at interior connections to columns. Mag Concr Res 2016;68(1):24–42.
- [20] Eder MA, Vollum RL, Elghazouli AY, Abdel-Fattah T. Modelling and experimental assessment of punching shear in flat slabs with shearheads. Engineering Structures. 2010 Dec 31;32(12):3911-24.
- [21] Yan PY, Wang YC. Hybrid steel tubular column/flat slab construction—Development of a shearhead system to improve punching shear resistance. Journal of Constructional Steel Research 2016;119:154-68.
- [22] Guandalini S, Burdet OL, Muttoni A. Punching tests of slabs with low reinforcement ratios. ACI Structural Journal 2009;106(1):87.
- [23] Muttoni A, Punching shear strength of reinforced concrete slabs without transverse reinforcement, ACI Structural Journal, 2008;105(4):440-450
- [24] fib - Fédération internationale du béton. Model Code 2010 – final draft, vol. 1 & vol. 2, fib Bulletins 65 & 66, Lausanne (Switzerland); 2012
- [25] DSS (Dassault Systèmes Simulia Corp). ABAQUS Analysis user's manual 6.14-2, DSS, Providence, RI, USA. 2014
- [26] Lubliner J, Oliver J, Oller S, Oñate E. A plastic-damage model for concrete. Int J Solids Struct 1989; vol. 25, pp. 299–326, 1989.
- [27] Lee JH, Fenves GL. Plastic-damage model for cyclic loading of concrete structures. J Eng Mech 1998; 124(8):892–900
- [28] EN 1992-1-1 - Eurocode 2: Design of concrete structures - Part 1-1: General rules and rules for buildings Brussels: European Committee for Standardization; December 2004.
- [29] Hordijk DA. Local approach to fatigue of concrete,” Doctorate dissertation. Delft, Netherlands. Delft University of Technology, 1991.
- [30] Baltay P, Gjelsvik A. Coefficient of Friction for Steel on Concrete at High Normal Stress. J Mater Civ Eng 1990;2(1):46-49.
- [31] Rabbat BG, Russell HG. Friction Coefficient of Steel on Concrete or Grout. J Struct Eng 1985;111(3):505–515.
- [32] EN 1993-1-1 - Eurocode 3: Design of steel structures - Part 1-1: General rules and rules for buildings Brussels: European Committee for Standardization; May 2005.

List of figures

Figure 1 Numerical models a) 3D overview, b) side view and mesh, c) concrete uniaxial model, d) steel model

Figure 2 Identification of constitutive and numerical parameters a) mesh size for HS13-00, b) mesh size for PG1 [22], c) tension stiffening response on PG1 [22], d) dilation angle ϕ for HS13-00, e) dilation angle ϕ for RC member PG1 [22], f) friction coefficient μ

Figure 3 General layout of hybrid members a) test setup, b) reinforcement layout, c) layout of sectors

Figure 4 Numerical validation of a) HS13-00 and HS03-00, b) HS13-00 and HS07-00, c) reinforcement strain for HS13, d) reinforcement strain for HS03-00.

Figure 5 comparison between damage zones obtained from numerical simulations against test crack patterns

Figure 6 Validation of RC flat slabs [22] a) PG2b, b) PG4, c) PG3, d) PG1, e) PG6, f) PG5

Figure 7 Characteristic dimensions for hybrid slabs a) cross-section view, b) top layout

Figure 8 Comparative results of parametric assessments: embedment length l_v a) $l_v/h_v=0.5$; $l_v/r_s=0.05$, b) $l_v/h_v=1.0$; $l_v/r_s=0.10$, c) $l_v/h_v=2.3$; $l_v/r_s=0.24$, d) $l_v/h_v=3.7$; $l_v/r_s=0.38$, e) $l_v/h_v=5.0$; $l_v/r_s=0.52$, f) $l_v/h_v=3.7$; $l_v/r_s=0.25$,

Figure 9 Cross-sectional damage patterns from numerical simulations a) $l_v/h_v=1.0$; $l_v/r_s=0.10$, b) $l_v/h_v=2.3$; $l_v/r_s=0.24$, c) $l_v/h_v=3.7$; $l_v/r_s=0.38$, d) $l_v/h_v=5.0$; $l_v/r_s=0.52$,

Figure 10 Comparative results of parametric assessments: effective depth d and embedment length l_v a) $d/r_s=0.15$, $l_v/h_v=1.0$, $l_v/r_s=0.1$; b) $d/r_s=0.24$, $l_v/h_v=1.0$, $l_v/r_s=0.1$; c) $d/r_s=0.15$, $l_v/h_v=3.7$, $l_v/r_s=0.38$; d) $d/r_s=0.24$, $l_v/h_v=3.7$, $l_v/r_s=0.38$; shear-head section size e) H60 $d/r_s=0.18$, $l_v/h_v=6.2$, $l_v/r_s=0.38$; f) H80 $d/r_s=0.18$, $l_v/h_v=4.6$, $l_v/r_s=0.38$

Figure 11 Tension damage kinematics for members with low h_v/d a) damage pattern after development of a slip crack, b) damage pattern at failure

Figure 12 Influence of f_c on the performance of hybrid slabs

Figure 13 Comparison between numerical and analytical $V - \psi$ a) $l_v/h_v=2.3$, b) $l_v/h_v = 3$

Figure 14 Comparative assessment of shear-head characteristics against predictions

Figure 15 Force distribution on the shear-head with the following embedment length l_v a) 100 mm, b) 230 mm, c) 370 mm, d) 500 mm

Figure 16 Prediction of Equations (11) and (12) in relationship with numerical results ($V_{u,num}$ – ultimate strength, $V_{yv,num}$ – yielding of the top flange)

Figure 17 Predictions of Equation (7) and (8) as a function of the shear action V_i

Figure 18 Comparison between a) Predictions of Equation (6) and numerical results, b) Predictions of Equation (11) and (12) and numerical results

List of tables

Table 1. Details of hybrid specimens

Table 2. Details of RC members [22]

Table 3. Summary of parametric assessments

Nomenclature

Greek letters

δ - displacement response

ε – strain

ε_{cl} - crushing strain

η – shear-head distribution factor

κ – force distribution factor

λ_ψ – rotation coefficient

λ_m – flexibility factor

μ - steel-concrete friction coefficient

ρ_l – flexural reinforcement ratio

σ – stress

$\sigma_{c,max}$ – strut crushing strength

φ - dilation angle

ψ – rotation

ϵ - potential eccentricity

Lowercase latin letters

b_0 - control perimeter

b_c – column size

b_v - shear-head width

c_c, c_k – location of neutral axis

d - bending effective depth

d_0 - shear effective depth

d_{g0}, d_g – aggregate size

d_{vfb} – centroid of bottom flange

f_c – concrete strength

f_{ct} - tensile strength of concrete

f_{ys} – reinforcement yield strength

f_{yv} – shear-head yield strength

h - flat slab thickness

h_v - shear-head depth
 k_ψ – factor for failure criterion
 l_0 - critical length
 l_{ch} - characteristic length of the element
 l_m - mesh size
 l_v – shear-head embedded length
 m_i – moment action per unit width
 m_{Rk} - plastic moment of hybrid sectors
 m_{Rc} - plastic moment of concrete sectors
 n_v – number of shear-heads
 $r_c = 2b_c/\pi$ and $b_c = (b_{c1} + b_{c2})/2$ (for rectangular columns)
 r_e – exterior slab radius
 r_s - slab radius (loading radius)
 w_i, w_{max} - the crack displacement
Uppercase latin letters
 A_{vv} – shear-head shear active area
 E_c - elastic concrete modulus
 E_s, E_v - steel elastic modulus
 G_c - crushing energy
 K_c – factor for the shape of the deviatoric plane
 L – specimen size
 $M_{v,i}$ - moment carried by one shear-head
 V - load
 V_e - volume of the mesh element
 V_{flex} - is the flexural strength
 V_i - is the shear action
 V_{test} -test ultimate strength
 $V_{u,num}$ - numerical ultimate strength
 $V_{yv,num}$ – shear-head yielding in numerical simulations
 $W_{v,pl}$ – shear-head plastic section modulus

Tables

Table 1. Details of hybrid specimens

| Member | $L_1=L_2$ (mm) | h (mm) | c_1/c_2 (mm) | d (mm) | ρ_l (%) | f_{yt} (MPa) | f_c (MPa) | l_v (mm) | d_v (mm) | $f_{yv,\rho}/f_{yv,w}$ (MPa) | V_{test} (kN) | $V_{u,num}$ (kN) | $V_{test}/V_{u,num}$ (-) |
|----------|-------------------|-------------|-------------------|-------------|--------------|-------------------|----------------|---------------|---------------|---------------------------------|--------------------|---------------------|--------------------------|
| HS13-00 | 2200 | 225 | 240/280 | 177 | 1.38 | 536 | 29 | 370 | 102 | 457/331 | 1005 | 994 | 1.01 |
| HS13-C0* | 2200 | 225 | 240/280 | 175 | 1.38 | 536 | 36.5 | 370 | 102 | 457/331 | 991 | 975 | 1.02 |
| HS07-C0* | 2200 | 225 | 240/280 | 175 | 0.75 | 565 | 39.2 | 370 | 102 | 457/331 | 880 | 894 | 0.98 |
| HS03-00 | 2200 | 225 | 240/280 | 178 | 0.33 | 547 | 37.5 | 370 | 102 | 457/331 | 582 | 599 | 0.97 |
| | | | | | | | | | | | | AVG | 1.00 |
| | | | | | | | | | | | | COV | 0.02 |

*C – continuity plate around the column

Table 2. Details of RC members [22]

| | $L_1=L_2$ (mm) | b_c (mm) | ρ_l (%) | d (mm) | f_c (MPa) | V_{test} (kN) | $V_{u,num}$ (kN) | $V_{test}/V_{u,num}$ (-) |
|------|-------------------|---------------|-----------------|-------------|----------------|--------------------|---------------------|--------------------------|
| PG3 | 6000 | 520 | 0.33 | 456 | 32.4 | 2153 | 2218 | 0.97 |
| PG1 | 3000 | 260 | 1.50 | 210 | 27.7 | 1023 | 991 | 1.03 |
| PG11 | 3000 | 260 | 0.75 | 210 | 31.5 | 763 | 775 | 0.98 |
| PG2b | 3000 | 260 | 0.25 | 210 | 40.5 | 440 | 458 | 0.96 |
| PG4 | 3000 | 260 | 0.25 | 210 | 32.2 | 408 | 448 | 0.91 |
| PG5 | 3000 | 260 | 0.33 | 210 | 29.3 | 550 | 528 | 1.04 |
| PG10 | 3000 | 260 | 0.33 | 210 | 28.5 | 540 | 533 | 1.01 |
| PG6 | 1500 | 130 | 1.50 | 96 | 34.7 | 238 | 230 | 1.04 |
| PG7 | 1500 | 130 | 0.75 | 100 | 34.7 | 241 | 220 | 1.09 |
| PG8 | 1500 | 130 | 0.33 | 117 | 34.7 | 140 | 149 | 0.94 |
| PG9 | 1500 | 130 | 0.25 | 117 | 34.7 | 115 | 125 | 0.92 |
| | | | | | | | AVG | 0.99 |
| | | | | | | | STDEV | 0.06 |
| | | | | | | | COV | 0.06 |

Table 3. Summary of parametric assessments

| | <i>Investigation</i> | l_v (mm) | <i>type (-)</i> | r_s (mm) | d (mm) | d_o (mm) | f_c (M Pa) | ρ_l (%) |
|----------------------------|--------------------------------|---------------|-----------------|---------------|-------------|---------------|--------------------|--------------|
| Embedment length | D177- L05 -H100-C29 | 50 | HEB100 | 964 | 177 | 117 | 29 | 0.33 – 2.20 |
| | D177- L10 -H100-C29 | 100 | HEB100 | 964 | 177 | 117 | 29 | 0.33 – 2.20 |
| | D177- L23 -H100-C29 | 230 | HEB100 | 964 | 177 | 117 | 29 | 0.33 – 2.20 |
| | D177- L37 -H100-C29 | 370 | HEB100 | 964 | 177 | 117 | 29 | 0.33 – 2.20 |
| | D177- L50 -H100-C29 | 500 | HEB100 | 964 | 177 | 117 | 29 | 0.33 – 2.20 |
| Flexibility | F2 -D177-L37-H100-C29 | 370 | HEB100 | 1500 | 177 | 117 | 29 | 0.33 – 2.20 |
| Effective depth | D140 -L10-H100-C29 | 100 | HEB100 | 964 | 140 | 92 | 29 | 0.33 – 2.20 |
| | D230 -L10-H100-C29 | 100 | HEB100 | 964 | 230 | 135 | 29 | 0.33 – 2.20 |
| | D280 -L10-H100-C29 | 100 | HEB100 | 964 | 280 | 152 | 29 | 0.33 – 2.20 |
| | D330 -L10-H100-C29 | 100 | HEB100 | 964 | 300 | 180 | 29 | 0.33 – 2.20 |
| | D140 -L37-H100-C29 | 370 | HEB100 | 964 | 140 | 92 | 29 | 0.33 – 2.20 |
| | D230 -L37-H100-C29 | 370 | HEB100 | 964 | 230 | 135 | 29 | 0.33 – 2.20 |
| | D280 -L37-H100-C29 | 370 | HEB100 | 964 | 280 | 152 | 29 | 0.33 – 2.20 |
| | D330 -L37-H100-C29 | 370 | HEB100 | 964 | 300 | 180 | 29 | 0.33 – 2.20 |
| Shear-head section size | D177-L37- H60 -C29 | 370 | H60 | 964 | 177 | 86 | 29 | 0.33 – 2.20 |
| | D177-L37- H80 -C29 | 370 | H80 | 964 | 177 | 95 | 29 | 0.33 – 2.20 |
| | D177-L37- H120 -C29 | 370 | HEB120 | 964 | 177 | 113 | 29 | 0.33 – 2.20 |
| Concrete strength | D177-L37-H100- C40 -C29 | 370 | HEB100 | 964 | 177 | 117 | 40 | 0.33 – 2.20 |
| | D177-L37-H100- C60 -C29 | 370 | HEB100 | 964 | 177 | 117 | 60 | 0.33 – 2.20 |
| | D177-L37-H100- C80 -C29 | 370 | HEB100 | 964 | 177 | 117 | 80 | 0.33 – 2.20 |

a) *Bold letter depict variables in the parametric investigation*

b) *Cross-sectional dimensions ($b \times t_f / d \times t_w / A_v / I_v$):*

H 60: 100mm×8mm / 100mm×5mm / 1180 mm² / 68.9×10⁴ mm⁴

H 80: 80mm×9mm / 100mm×5.5mm / 1780 mm² / 193.4×10⁴ mm⁴

HEB 100: 100mm×10mm / 100mm×6mm / 2600 mm² / 449.5×10⁴ mm⁴

HEB 120: 120mm×11mm / 100mm×6.5mm / 3400 mm² / 864.4×10⁴ mm⁴

Figures

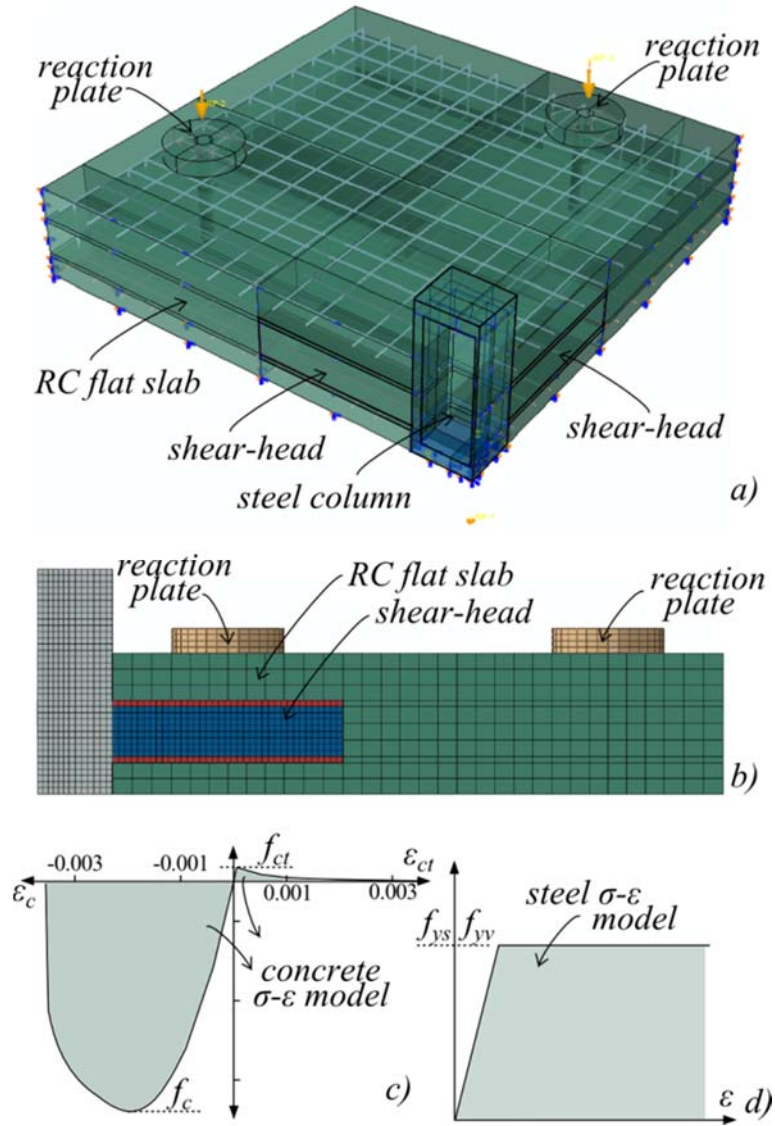


Figure 1 Numerical models a) 3D overview, b) side view and mesh, c) concrete uniaxial model, d) steel model

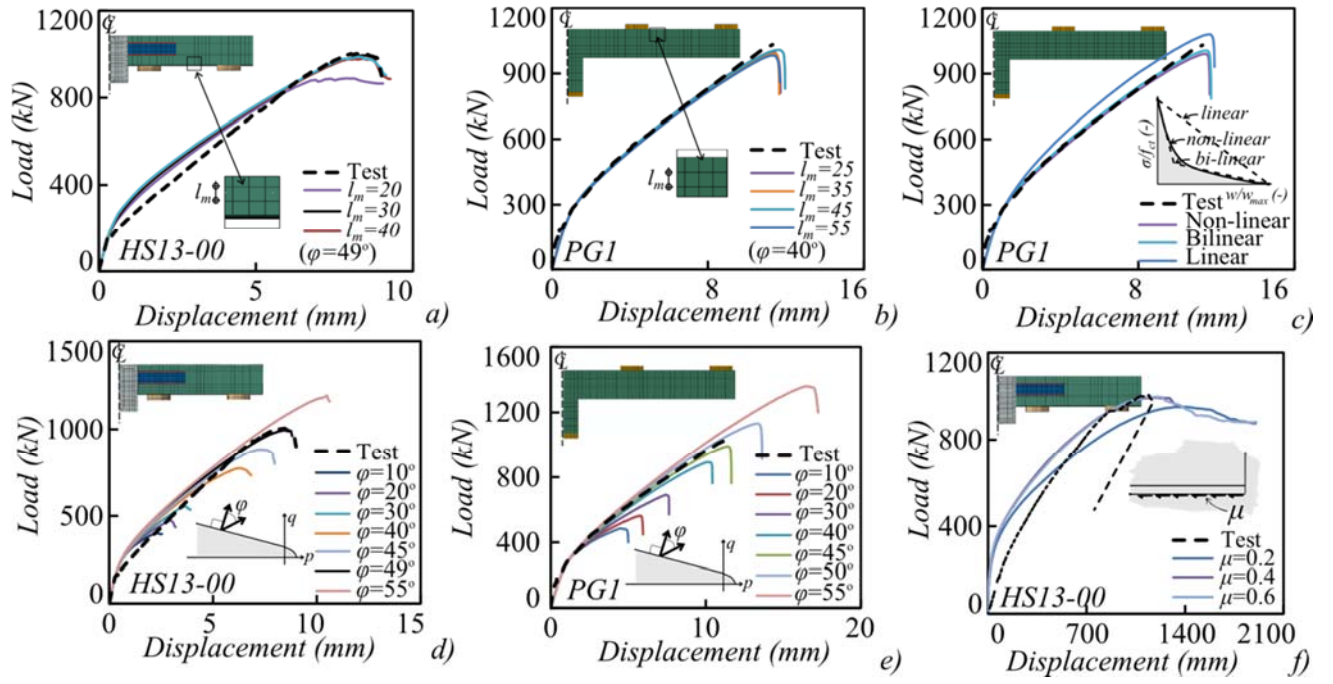


Figure 2 Identification of constitutive and numerical parameters: a) mesh size for HS13-00, b) mesh size for PG1 [22], c) tension stiffening response on PG1 [22], d) dilation angle φ for HS13-00, e) dilation angle φ for RC member PG1 [22], f) friction coefficient μ

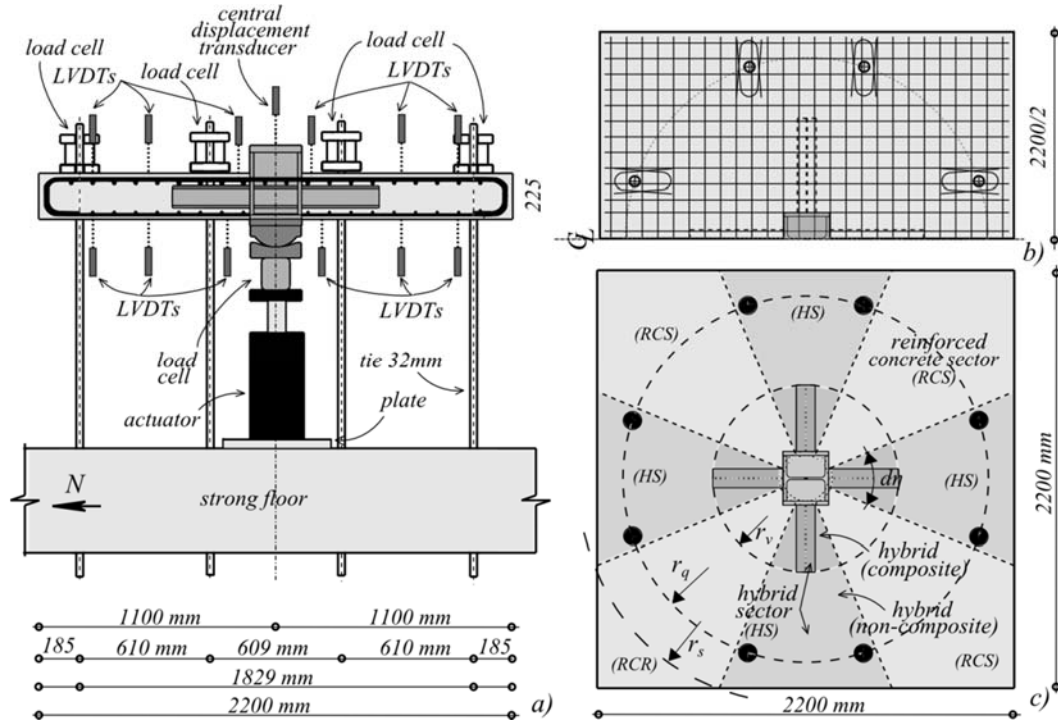


Figure 3 General layout of hybrid members a) test setup, b) reinforcement layout, c) layout of sectors

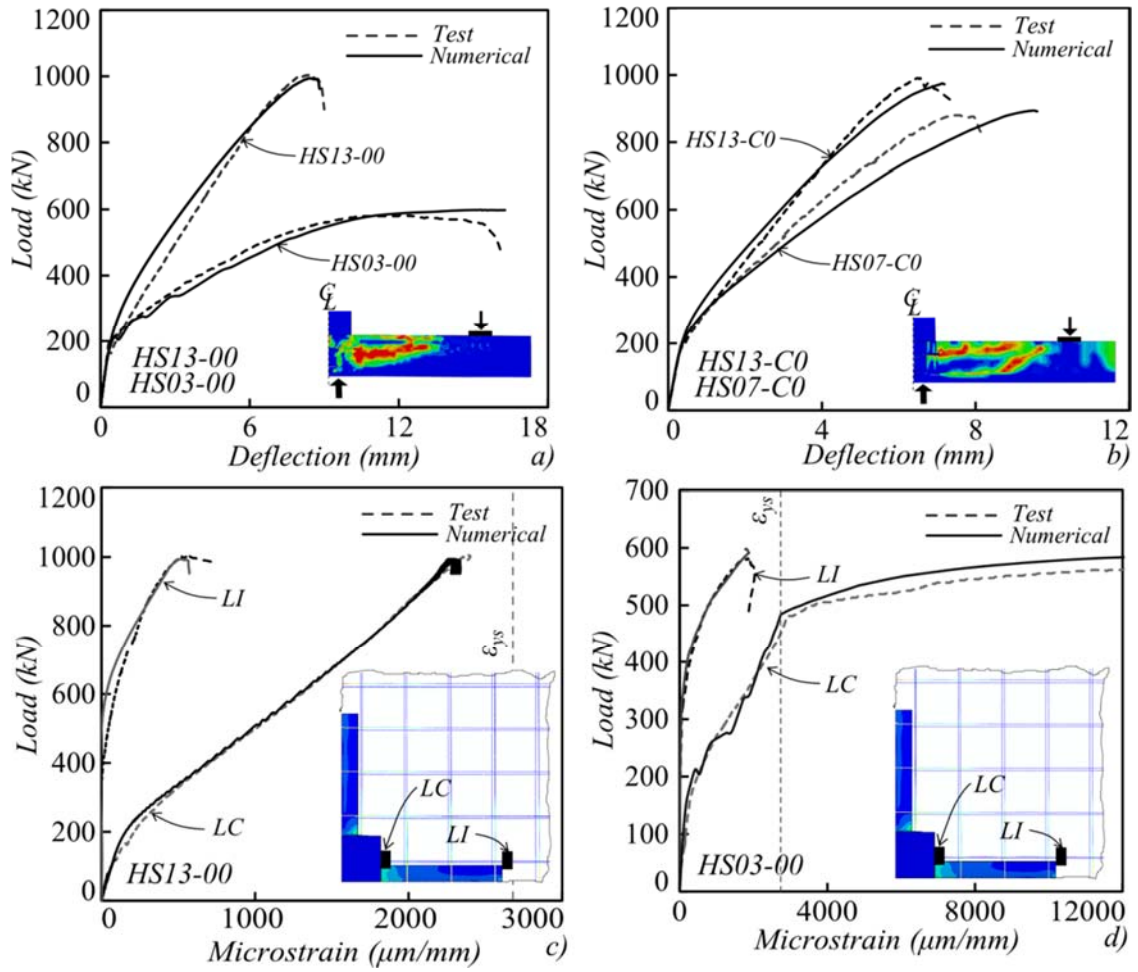


Figure 4 Numerical validation of a) HS13-00 and HS03-00, b) HS13-00 and HS07-00, c) reinforcement strain for HS13, d) reinforcement strain for HS03-00.

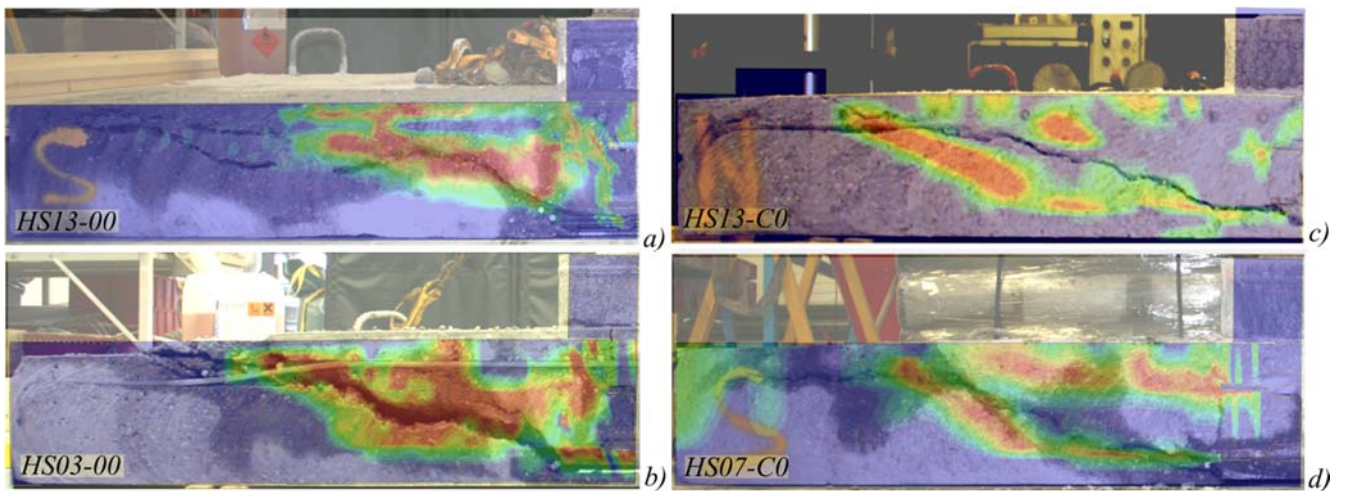


Figure 5 Comparison between damage zones obtained from numerical simulations against test crack patterns

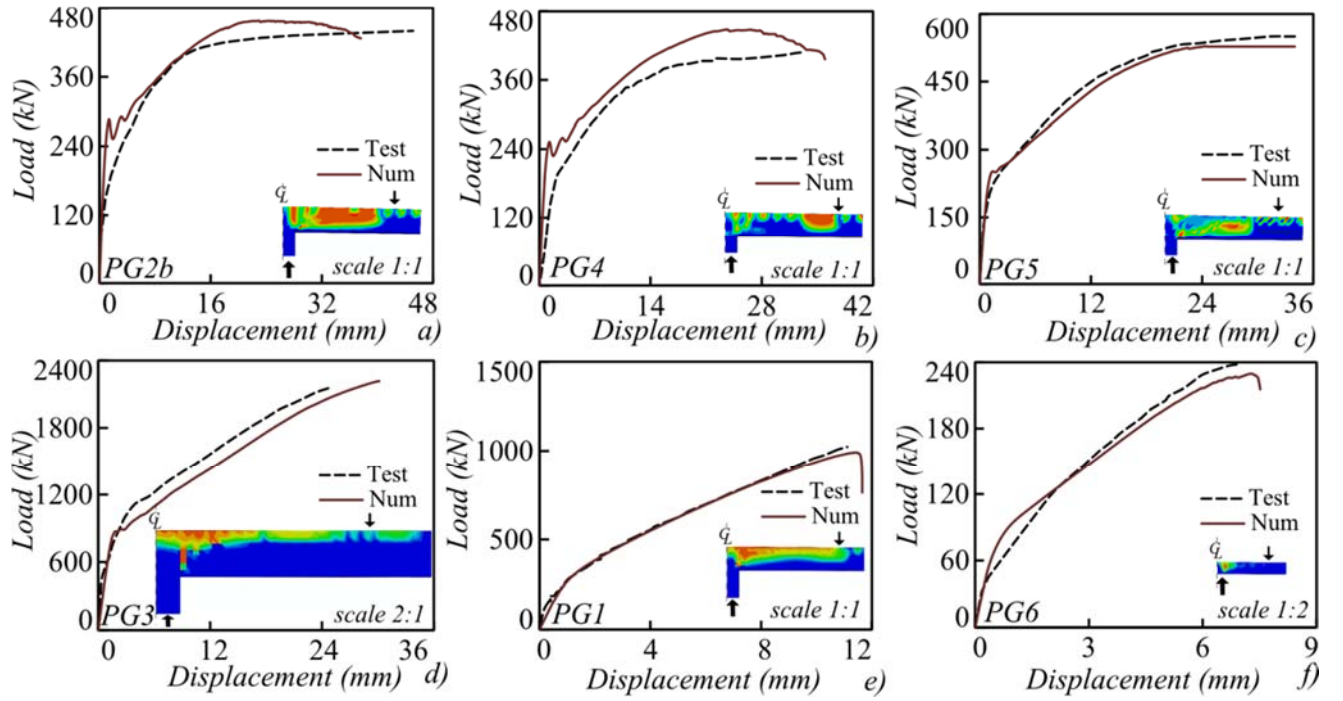


Figure 6 Validation of RC flat slabs [22] a) PG2b, b) PG4, c) PG3, d) PG1, e) PG6, f) PG5

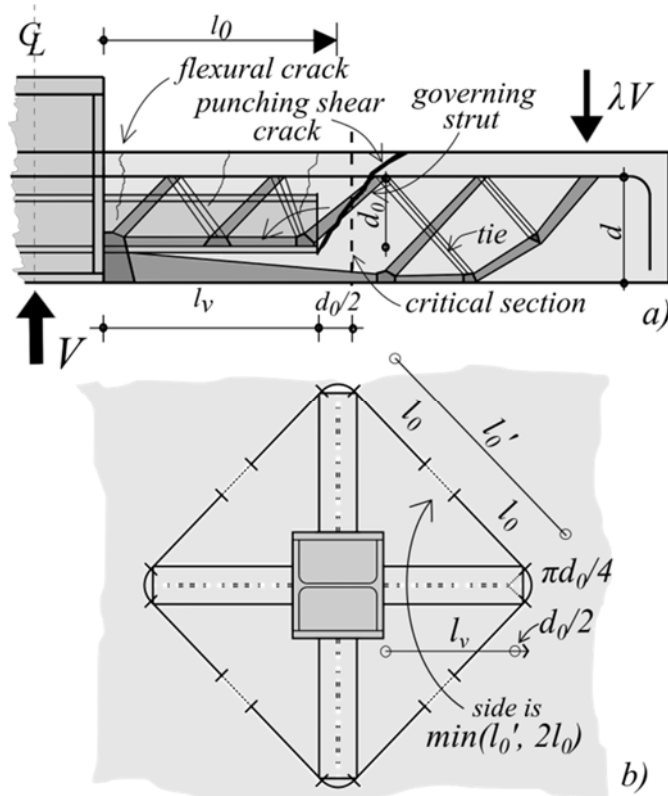


Figure 7 Characteristic dimensions for hybrid slabs a) cross-section view, b) top layout

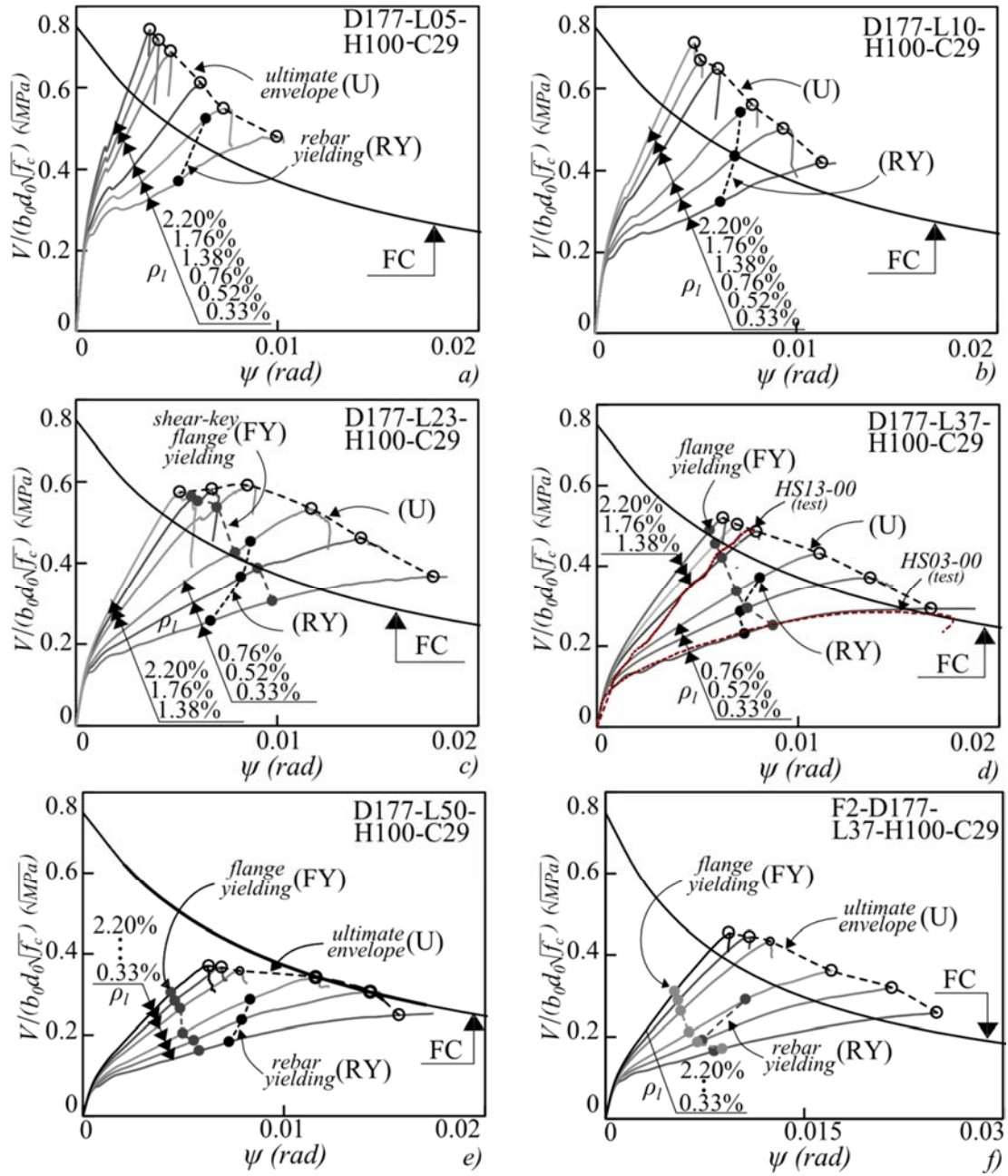


Figure 8 Comparative results of parametric assessments: embedment length l_v : a) $l_v/h_v=0.5$; $l_v/r_s=0.05$, b) $l_v/h_v=1.0$; $l_v/r_s=0.10$, c) $l_v/h_v=2.3$; $l_v/r_s=0.24$, d) $l_v/h_v=3.7$; $l_v/r_s=0.38$, e) $l_v/h_v=5.0$; $l_v/r_s=0.52$, f) $l_v/h_v=3.7$; $l_v/r_s=0.25$.

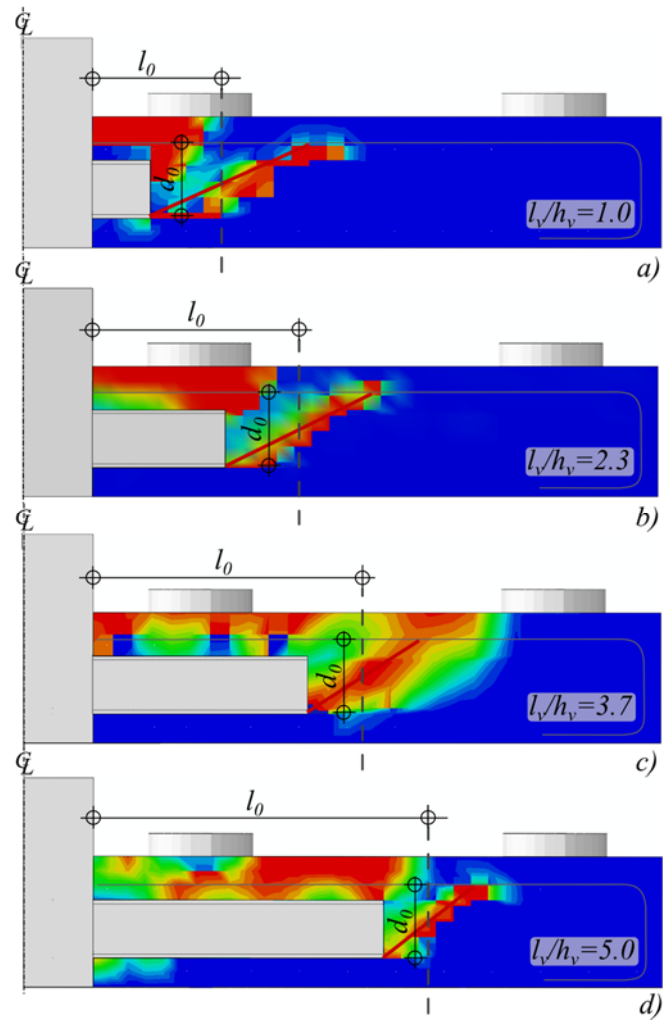


Figure 9 Cross-sectional damage patterns from numerical simulations a) $l_v/h_v=1.0$; $l_v/r_s=0.10$, b) $l_v/h_v=2.3$; $l_v/r_s=0.24$, c) $l_v/h_v=3.7$; $l_v/r_s=0.38$, d) $l_v/h_v=5.0$; $l_v/r_s=0.52$.

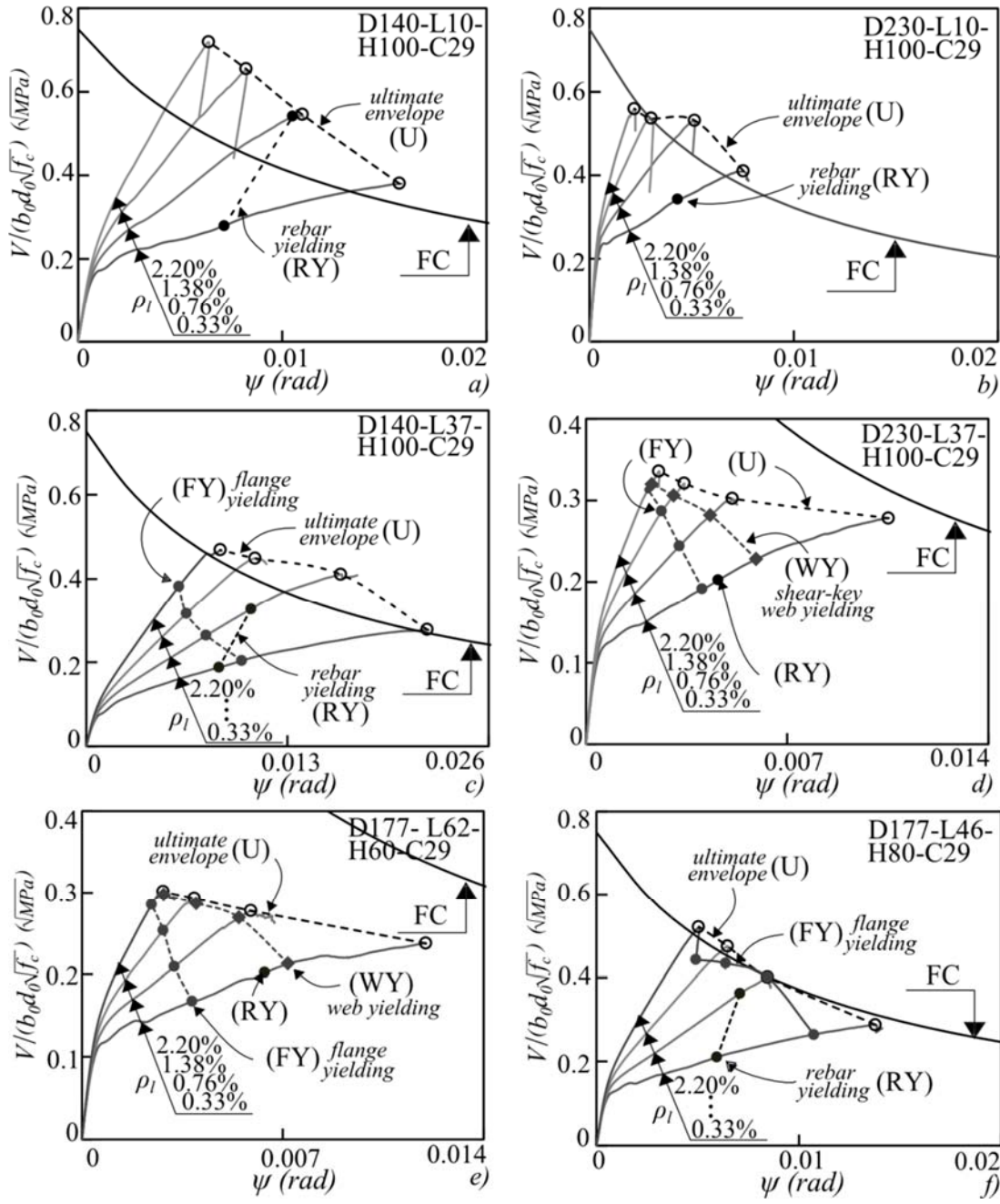


Figure 10 Comparative results of parametric assessments: effective depth d and embedment length l_v : a) $d/r_s=0.15$, $l_v/h_v=1.0$, $l_v/r_s=0.1$; b) $d/r_s=0.24$, $l_v/h_v=1.0$, $l_v/r_s=0.1$; c) $d/r_s=0.15$, $l_v/h_v=3.7$, $l_v/r_s=0.38$; d) $d/r_s=0.24$, $l_v/h_v=3.7$, $l_v/r_s=0.38$; shear-head section size e) H60 $d/r_s=0.18$, $l_v/h_v=6.2$, $l_v/r_s=0.38$; f) H80 $d/r_s=0.18$, $l_v/h_v=4.6$, $l_v/r_s=0.38$.

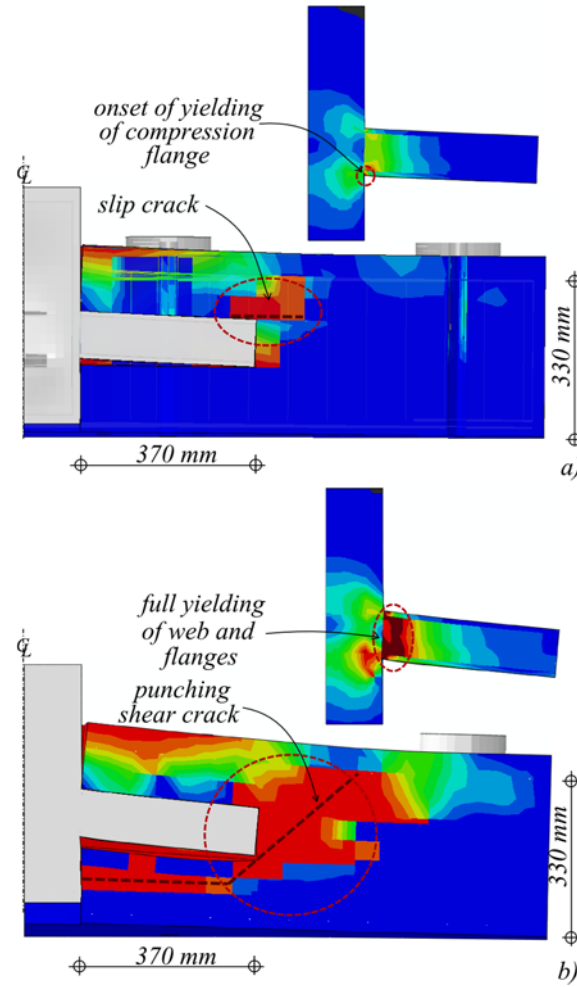


Figure 11 Tension damage kinematics for members with low h_v/d a) damage pattern after development of a slip crack, b) damage pattern at failure

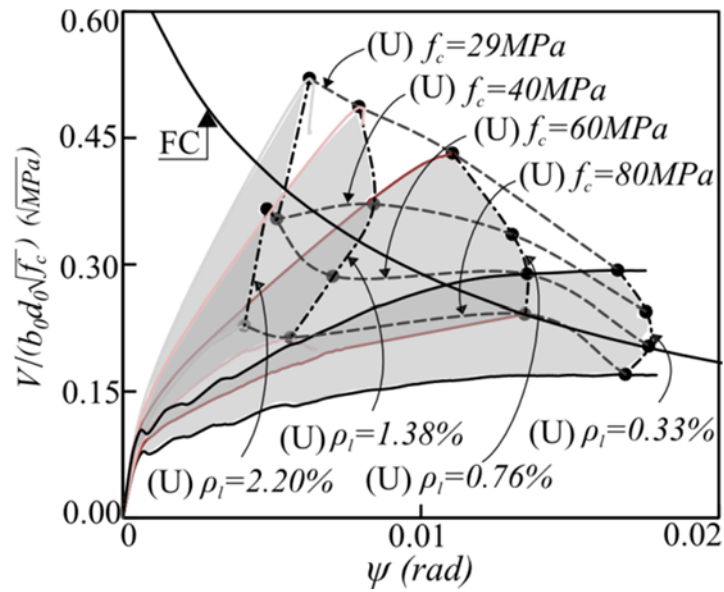


Figure 12 Influence of f_c on the performance of hybrid slabs

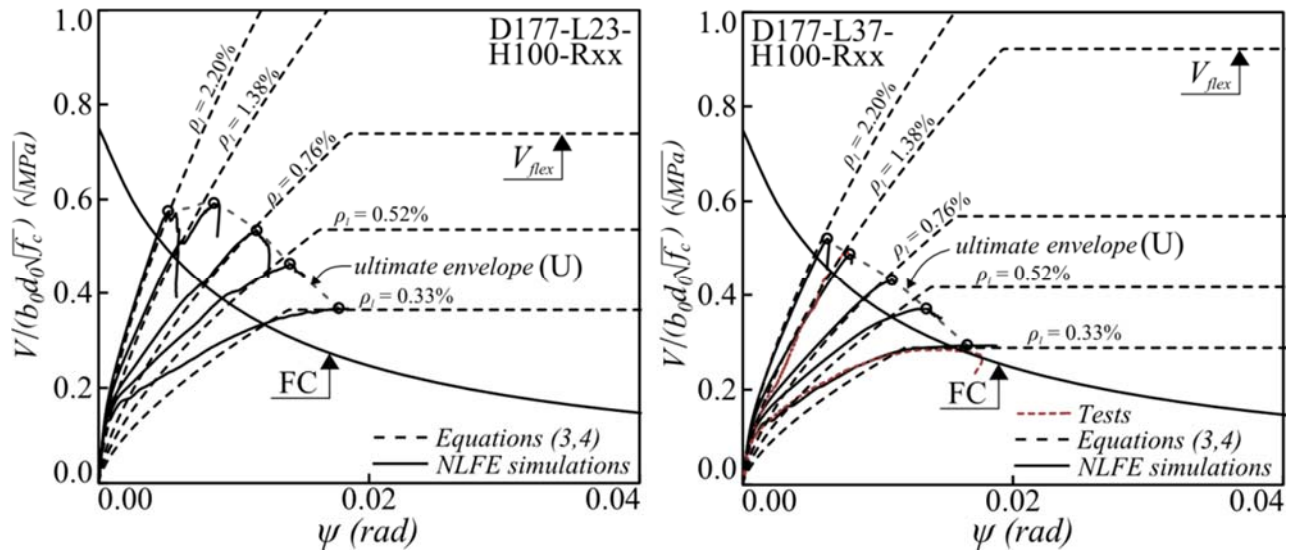


Figure 13 Comparison between numerical and analytical $V - \psi$ a) $l_v/h_v=2.3$, b) $l_v/h_v = 3.7$

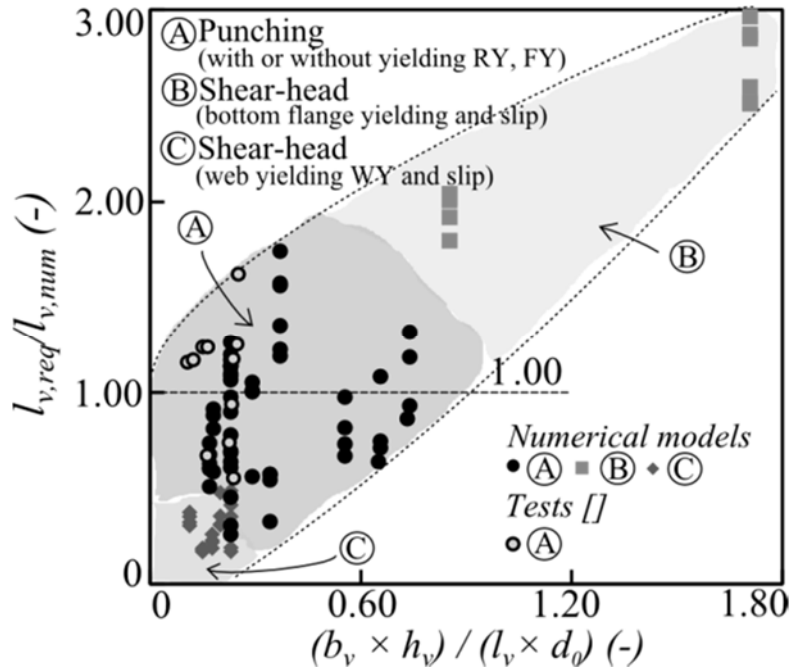


Figure 14 Comparative assessment of shear-head characteristics against predictions

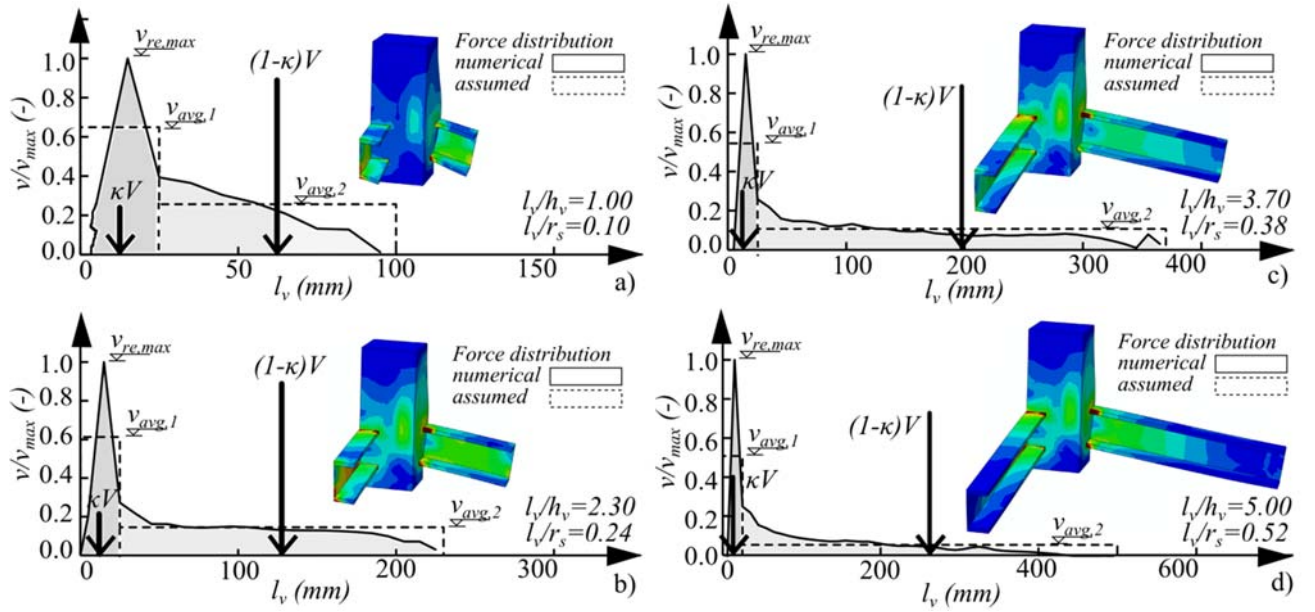


Figure 15 Force distribution on the shear-head with the following embedment length l_v : a) 100 mm, b) 230 mm, c) 370 mm, d) 500 mm

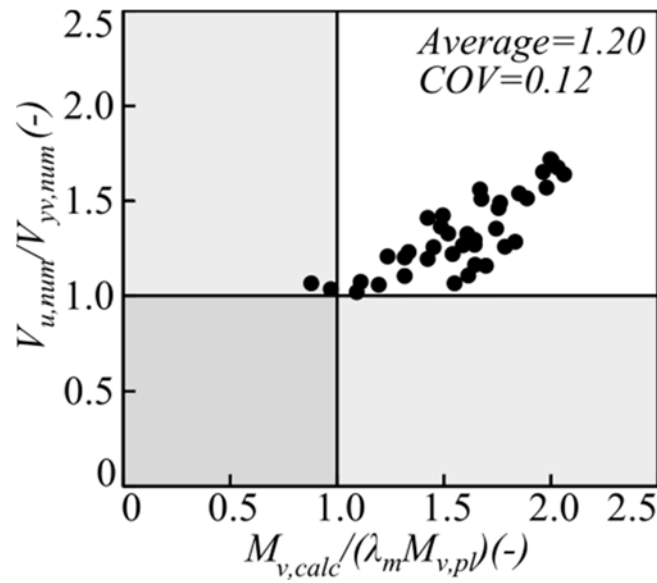


Figure 16 Prediction of Equations (11) and (12) in relationship with numerical results ($V_{u,num}$ = ultimate strength, $V_{yv,num}$ = yielding of the top flange)

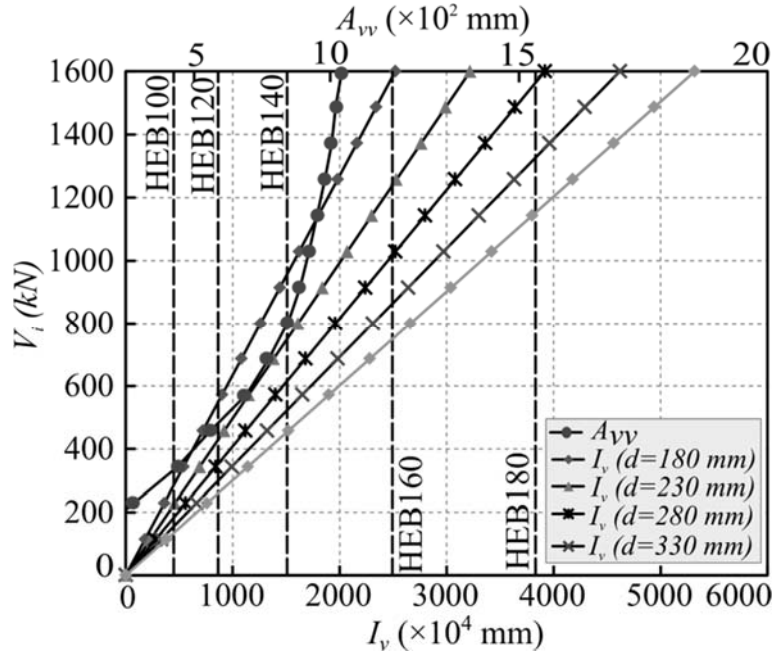


Figure 17 Predictions of Equation (7) and (8) as a function of the shear action V_i

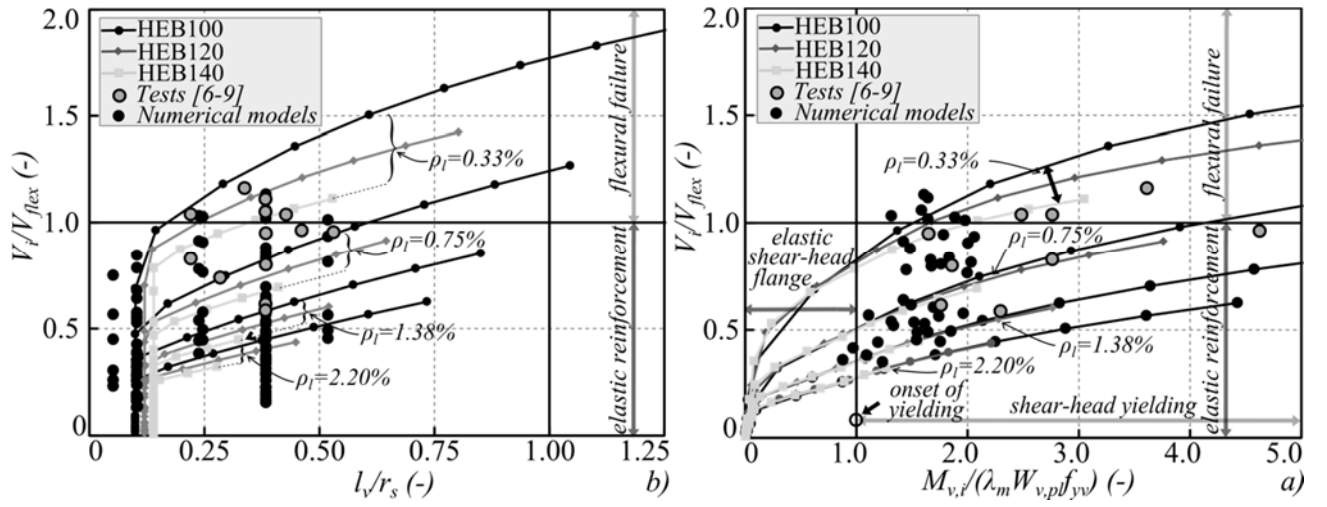


Figure 18 Comparison between a) Predictions of Equation (6) and numerical results, b) Predictions of Equation (11) and (12) and numerical results.